AIP | Physics of Fluids

Stratified spin-up in a sliced, square cylinder

R. J. Munro and M. R. Foster

Citation: Physics of Fluids **26**, 026603 (2014); doi: 10.1063/1.4864266
View online: http://dx.doi.org/10.1063/1.4864266
View Table of Contents: http://scitation.aip.org/content/aip/journal/pof2/26/2?ver=pdfcov
Published by the AIP Publishing

PHYSICS OF FLUIDS **26**, 026603 (2014)

Stratified spin-up in a sliced, square cylinder

R. J. Munro[1] and M. R. Foster[2]
[1]*Faculty of Engineering, University of Nottingham, Nottingham NG7 2RD, United Kingdom*
[2]*Department of Mathematical Sciences, Rensselaer Polytechnic Institute, Troy, New York 12180, USA*

(Received 11 December 2013; accepted 21 January 2014; published online 18 February 2014)

We previously reported experimental and theoretical results on the linear spin-up of a linearly stratified, rotating fluid in a uniform-depth square cylinder [M. R. Foster and R. J. Munro, "The linear spin-up of a stratified, rotating fluid in a square cylinder," J. Fluid Mech. **712**, 7–40 (2012)]. Here we extend that analysis to a "sliced" square cylinder, which has a base-plane inclined at a shallow angle α. Asymptotic results are derived that show the spin-up phase is achieved by a combination of the Ekman-layer eruptions (from the perimeter region of the cylinder's lid and base) and cross-slope-propagating stratified Rossby waves. The final, steady state limit for this spin-up phase is identical to that found previously for the uniform depth cylinder, but is reached somewhat more rapidly on a time scale of order $E^{-1/2}\Omega^{-1}/\log(\alpha/E^{1/2})$ (compared to $E^{-1/2}\Omega^{-1}$ for the uniform-depth cylinder), where Ω is the rotation rate and E the Ekman number. Experiments were performed for Burger numbers, S, between 0.4 and 16, and showed that for $S \gtrsim \mathcal{O}(1)$, the Rossby modes are severely damped, and it is only at small S, and during the early stages, that the presence of these wave modes was evident. These observations are supported by the theory, which shows the damping factors increase with S and are numerically large for $S \gtrsim \mathcal{O}(1)$. [http://dx.doi.org/10.1063/1.4864266]

I. INTRODUCTION

A quite thorough understanding of the way in which rapidly rotating fluids, in axisymmetric containers, adjust to small changes in rotation rates – either "spin-up" or "spin-down" – has developed over the past 50 or so years. However, our understanding of asymmetric spin-up is still incomplete. The seminal work on axisymmetric spin-up is by Greenspan and Howard,[1] and the large number of subsequent investigations has been summarized in the review articles first by Benton and Clark[2] and more recently by Duck and Foster.[3] For a homogeneous fluid, we know that an increase in rotation rate of the container results in the formation of thin, quasi-steady viscous Ekman layers at the horizontal lid and base, within which layers the spun-up fluid is transported radially outward, where it erupts into the vertical, sidewall Stewartson layers.[1,4] The fluid then flows radially inward as it exits the Stewartson layers, completing the meridional circuit.[4] As the fluid negotiates this closed path, it advects with it the spun-up fluid from the layers near the walls. The result is an exponential adjustment to the new rotation rate, on the so-called "spin-up timescale" (which will be defined below). Here we are interested in how the combined effects of fluid stratification and an inclined base affect the spin-up process in a container of square cross-section.

In the case of a continuously stratified fluid, apart from the definitive work by Walin[5] and Sakurai,[6] few investigations have been conducted, and most of those are for uniform-depth axisymmetric containers. Walin showed that the Ekman-layer fluid, on reaching the sidewall, cannot flow up the wall, that motion being suppressed by gravity. Instead, it erupts into the core at short times. Moreover, at the end of the spin-up time scale, the fluid is not yet spun up, the final state of near-solid rotation being reached on a much longer diffusive time scale. It has been shown that a stratified two-layer fluid in a container whose walls have discontinuous slopes exhibits an algebraic rather

than exponential adjustment to a new rotation rate.[7] Spin-up (-down) in a continuously stratified fluid in a smooth conical container was found to lead to a variety of differing behaviours, depending of relative sizes of the dimensionless parameters of the problem, including finite-time singularities, long-time steady flow, slope currents, and centrifugal instability.[8,9]

Due to its relevance to models of large-scale ocean circulations, and in particular in simulating β-plane effects, Pedlosky and Greenspan[10] considered the spin-up of a homogeneous fluid in a circular cylinder with a linearly sloping bottom boundary (a configuration commonly referred to as a "sliced" cylinder). Two cases were considered, where the relative flow was either driven by a uniform increase in the container's rotation rate, or by the steady, differential rotation of the container's (horizontal) lid. Of most relevance to the present study is the former case, where it was shown that the uniform increase in rotation rate causes the relative motion of fluid columns across the base slope (along lines of constant height) resulting in the production of Rossby waves. For the case where the base slope is small (but with the slope height large compared to the thickness of the Ekman layer), it was shown that the relative vorticity induced by Ekman suction is insignificant compared to that produced by the Rossby waves, and so these Rossby waves play the dominant role in the fluid's spin-up.

Research into spin-up in non-axisymmetric containers was begun by van Heijst,[11] who used experiments to analyze the nonlinear spin-up from rest of a free-surface fluid in several geometries, including a semi-circular cylinder and an annular cylinder with a radial barrier. Following this, van Heijst and colleagues studied the spin-up from rest of both homogeneous and linearly stratified fluids in a uniform-depth rectangular container (with horizontal aspect ratios of between 2 and 5).[12] This work was later extended to the case of an homogeneous fluid in a rectangular container with an inclined base plane.[13] All of these studies found that the fluid's adjustment to solid rotation is characterised by three key stages, which are here summarised in relation to the case of a uniform-depth rectangular container.[12] There is, to begin, an inviscid starting flow which has zero absolute vorticity relative to the inertial frame. In the co-rotating reference frame the early flow takes the form of an anticyclonic cell with closed streamlines that fill the flow domain. During the second stage the boundary layers are established and in the case of no stratification, the anticyclonic starting-vortex is stretched by Ekman suction. Moreover, the boundary layers along each sidewall are observed to separate and detach near the corner regions, leading to the formation of corner cells consisting of vertical, cyclonic line vortices which extend over the tank depth. The cells downstream of the two long sides subsequently grow and interact with the central anticyclonic cell, giving rise to a three-dimensional, chaotic flow structure within the interior region. During the final stage, and for the case of a uniform-depth container, the background rotation leads to an eventual transition to two-dimensional motion, resulting in the formation of an organised flow pattern consisting of an array of alternately cyclonic and anticyclonic cells, which gradually decay as the fluid is spun-up (and spun-down) by the Ekman layer below each cell. For the case of a sloped-based rectangular container, this final, organized pattern occurs only when the bottom slope is small; for steeper slopes the relative fluid motion was observed to remain unsteady and irregular, eventually decaying on a diffusive time scale.[13]

Recently, the authors of this paper reported experimental and asymptotic results for the spin-up of a linearly stratified fluid in a closed, uniform-depth cylinder of square cross-section.[14] We found a number of interesting features not noted in stratified spin-up in axisymmetric containers: (a) Fluid in the horizontal-wall Ekman layers collides with the vertical walls in the corners, and erupts into the interior, even on the spin-up time scale. (b) The vertical-wall boundary layers are not buoyancy layers, but rather conventional Prandtl boundary layers on the horizontal velocity, and are fully nonlinear even for very small Rossby numbers. (c) Due to finite-time boundary-layer singularity formation, cyclonic eddies form in the vertical corner regions of the container, and that formation occurs for times that scale with the inverse Rossby number.

These results stand in contrast with what is known about the spin-up of a linearly stratified fluid in a axisymmetric container: (a) Unless there is long-time differential rotation between the horizontal and vertical walls,[15] there is no Ekman layer eruption on the spin-up time scale. (b) The vanishing of the radial velocity component at the vertical wall means that the tangential Coriolis force is zero there as well, so therefore the tangential velocity component also vanishes at the boundary, and the

vertical-wall boundary layer takes the vertical velocity to zero at the wall, in a "buoyancy layer." (c) The circular perimeter of the vertical boundary means there is no eddy formation for sufficiently small Rossby numbers.

In a square cylinder of width L, containing linearly stratified fluid with buoyancy frequency N, which is spun-up from a rotation rate of $\Omega - \Delta\Omega$ to Ω, the characteristic parameters that describe the motion are the Ekman (E), Rossby (ϵ), and Burger (S) numbers, defined as

$$E \equiv \frac{\nu}{\Omega L^2}, \quad \epsilon \equiv \frac{\Delta\Omega}{\Omega}, \quad S \equiv \left(\frac{N}{\Omega}\right)^2,$$

where ν denotes the fluid's kinematic viscosity. There is, of course, a Schmidt number, but it has almost no dynamical significance for case considered here of salt (NaCl) in water.

In the asymptotic theory reported in Foster and Munro,[14] the fluid motion in a uniform-depth square cylinder was characterised by three time scales: $E^{-1/2}\Omega^{-1}$, the standard "spin-up" time scale; $\epsilon^{-1}\Omega^{-1}$, the formation time scale for the corner eddies; $E^{-1}\Omega^{-1}$, the diffusive time scale. The asymptotics presented there require that

$$\epsilon \ll E^{1/2} \ll 1, \tag{1}$$

and so, as a consequence, the theoretical results are based on the assumption that the formation of the cyclonic corner eddies occurs on a time scale that is much longer than the spin-up time scale. However, condition (1) is difficult to achieve in the laboratory, and $\epsilon \sim 10E^{1/2}$ is more typical of their experimental conditions. Despite this notable difference, a very good level of quantitative agreement was found between the theory and experimental data.

When we turn to the problem reported here, for the sliced square cylinder, an additional parameter, α, the inclination angle of the tank's base, affects the spin-up processes. There are now four time scales: $\alpha^{-1}\Omega^{-1}$, the time scale for stratified, Rossby-wave propagation across the tank; $E^{-1/2}\Omega^{-1}$, the spin-up time scale; $\epsilon^{-1}\Omega^{-1}$, the time for corner eddy formation; $E^{-1}\Omega^{-1}$, the diffusive time scale. We take these time scales to be ordered in the sequence listed, and that leads to the parametric restrictions on the asymptotics reported herein,

$$\epsilon \ll E^{1/2} \ll \alpha \ll 1. \tag{2}$$

In all of these spin-up problems, the nominal "spin-up time" is taken to be $E^{-1/2}\Omega^{-1}$, but as we shall see subsequently, in this geometrical configuration, that is not quite the case. The actual spin-up time scale that emerges is a bit shorter – it is $E^{-1/2}\Omega^{-1}/\log(\alpha/E^{1/2})$ – because of the sloped floor of the container. Nonetheless, in all of the formulation, $\alpha/E^{1/2}$ is taken to be order one, and then subsequently, in constructing the core solution, the relative ordering $\alpha/E^{1/2} \gg 1$ is applied. So, for simplicity in paper organization, $E^{-1/2}\Omega^{-1}$ is sometimes referred to, for brevity, as the "spin-up time"—even though a slightly different timescale actually arises in the analysis. However, as this new spin-up time emerges, requirements that the series in α and E be an asymptotic series leads to a quite severe requirement, that

$$\frac{1}{\log(\alpha/E^{1/2})} \ll 1,$$

which is extremely difficult to realize in the laboratory. If one chooses $\alpha = o(E^{1/2})$ instead, the only affect of the slope is in the Ekman dynamics itself, and is therefore not interesting or significant.

In addition to these "distinguished" time scales, in both this problem and the former one,[14] there is an early-time behaviour, due to the impulsive start in a non-axisymmetric container. For completeness, this starting flow is also reported here; it provides the initial condition for the motion on the $\alpha^{-1}\Omega^{-1}$ time scale.

A key issue in this paper and in our previous, related paper,[14] is the eruption of fluid from the Ekman layer. If (u, v) denote horizontal velocity components – either Cartesian or polar – made dimensionless with $\epsilon\Omega L$, then the dimensionless Ekman flux in a direction d in a rotating reference

frame, in which the walls are at rest, is

$$\mathcal{F}_d = -\frac{1}{2}E^{1/2}\big(v+u\big), \tag{3}$$

where d is radial for circular symmetry, or x, say, in a Cartesian geometry. In the axisymmetric case, Walin points out that the Ekman-layer eruption occurs over a dimensionless region of width $tE^{1/2}$ (where time and lengths have been scaled by Ω^{-1} and L), so that on the spin-up time scale, the fluid exchange between the Ekman layer and the inviscid interior occurs over an order-one region.[5] Our situation is quite different, in that the tangential horizontal velocity component, v, does not vanish at the vertical wall at x = 0, for example, and hence there is non-zero Ekman flux into the corner on the spin-up time scale, which must erupt into the interior. Accounting for these eruptions is an essential ingredient in getting the flow dynamics correct.

A parametric restriction, in addition to (2), should be noted here. Application of the boundary condition on the sloping lower wall involves transferring the boundary condition to the flat coordinate plane, and corrections to that scale with α^2. Those corrections are ignored in the asymptotic theory constructed here, so their neglect as compared with the Ekman suction term leads to the requirement that α be not too big, that is,

$$\alpha \ll E^{1/4}. \tag{4}$$

It is pertinent here to highlight two key differences between the analysis presented here for sliced square cylinder, and that reported previously for the uniform-depth square cylinder: (a) The interior motion in the sliced cylinder is of two sorts – a geostrophic component that decays rapidly on the $\alpha^{-1}\Omega^{-1}$ time scale, and a component that may be understood to be stratified Rossby waves, which decay by interaction with the Ekman layers, on a longer time scale. (b) The decay of the two internal motions indicated above leads to a state for long "spin-up" times that is the same as that for the uniform-depth cylinder. The Rossby waves, occurring on a time scale $\alpha^{-1}\Omega^{-1}$, decay at a slightly elevated rate, namely, for $tE^{1/2}\log(\alpha/E^{1/2}) \gg 1$. That rate arises from the interplay of the inclined base and Ekman-layer eruption, and is manifest as a non-uniformity of the two-variable expansion procedure in Fourier space. We show that there must indeed be a logarithm in the time scale. Also note that the decay rates of the Rossby waves for $S \gtrsim \mathcal{O}(1)$ are numerically very large, making it virtually impossible to observe the waves under typical laboratory conditions.

In Sec. II we describe the experiments. In Sec. III we present the analysis of the interior motion on the time scales $\alpha^{-1}\Omega^{-1}$ and $E^{-1/2}\Omega^{-1}/\log(\alpha/E^{1/2})$. In particular, the Rossby waves and their decay are described in Secs. III F 2 and III F 3, respectively. For comparison, we also consider the limiting case for small-S in Sec. IV. The discussion of the side-wall Rayleigh layer in Sec. V makes possible quantitative comparisons of experimental and theoretical velocity-profiles, which are presented at the end of that section.

II. EXPERIMENTS

A. Apparatus and flow measurement techniques

The basic set-up is shown in Figure 1. Each experiment was performed in a sliced square cylinder (width $L = 38.0$ cm, mean depth $H = 48.6$ cm), with its base-plane inclined at angle $\alpha = 0.175$ rad (10°), and enclosed by a rigid horizontal lid. The cylinder was mounted on a variable-speed turntable, with its central axis coincident with the table's rotation axis, and completely filled with a linearly stratified salt-water solution of buoyancy frequency $N = \sqrt{g(\rho_m - \rho_\ell)/\rho_\ell H}$, where ρ_ℓ and $\rho_m > \rho_\ell$ are the fluid densities at the lid and mid-slope depth of the cylinder, respectively. Once filled, the cylinder was brought slowly, over a period of at least 12 h, from rest, to the initial steady rotation rate $\Omega - \Delta\Omega$, and then left for at least 24 h to allow the stratified salt-water solution to attain a state of near solid-rotation.

The experiment was then initiated (at time $t^* = 0$) by impulsively increasing the table's rotation rate from $\Omega - \Delta\Omega$ to Ω. The key parameters for each experiment are listed in Table I. Attention throughout was focused on the case of small Rossby number, $\epsilon = \Delta\Omega/\Omega = \mathcal{O}\left(10^{-2}\right)$. The Burger

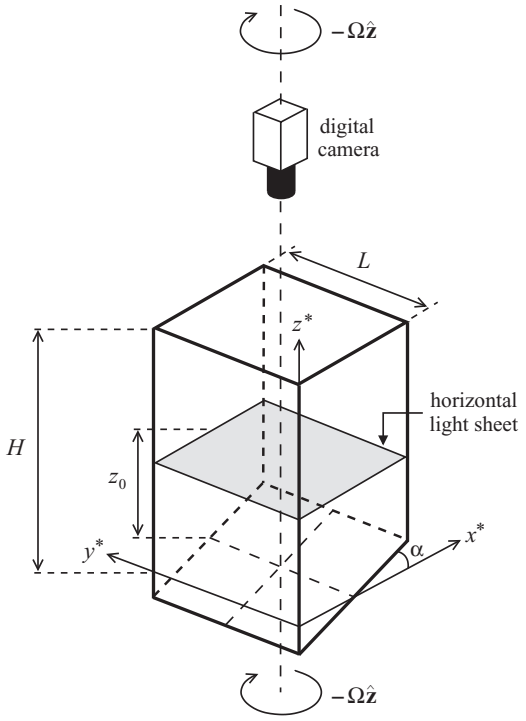

FIG. 1. Sketch of the experiment set-up.

number, $S = (N/\Omega)^2$, was varied between 0.4 and 16, and the Ekman number, $E = \nu/\Omega L^2$, was $\mathcal{O}\left(10^{-5}\right)$. For the range of dissolved-salt concentrations used here, the fluid's kinematic viscosity (ν) and salt diffusivity (κ) were constant, giving a constant Schmidt number $Sc = \nu/\kappa \approx 670$.[16] We also define here the aspect ratio, $h = H/L$, which was throughout fixed at $h = 1.28$. For reference purposes, we let (x^*, y^*, z^*) denote the coordinate system defined relative to the new rotating frame of the cylinder (see Figure 1) with the z^*-axis directed vertically upwards and with the mid-slope horizontal plane corresponding to $z^* = 0$. In this coordinate system the central rotation axis of the table (and cylinder) is located along (x^*, y^*, z^*) = ($L/2$, $L/2$, z^*), and the plane of the cylinder's base is defined by $z^* = (x^* - L/2)\tan\alpha$. Also note that the turntable was always set to rotate in the clockwise direction, so here we denote the final angular velocity of the cylinder by $\mathbf{\Omega} = -\Omega\hat{\mathbf{z}}$, so that $\Omega > 0$ ($\hat{\mathbf{z}}$ is the unit z-direction).

Measurements of the fluid's velocity field, as it adjusts to the increased rotation rate of the cylinder, were obtained using two-dimensional, particle imaging velocimetry (PIV). Small, tracer particles were added to the fluid during the filling process, and illuminated using a thin, horizontal light sheet directed through the cylinder's interior at the height corresponding to the mean neutral-buoyancy level of the particles, here denoted by z_0 (see Figure 1). In each experiment z_0 was set through the choice of ρ_ℓ and ρ_m. The relative motion of the tracer particles was recorded using a

TABLE I. The key parameters for each experiment.

Expt.	Ω (rad/s)	ϵ	S	$E^{1/2}$	z_0/H
A	0.209	0.0521	15.4	0.00575	0.144
B	0.351	0.0213	6.05	0.00444	0.267
C	0.429	0.0254	4.46	0.00402	0.329
D	0.443	0.0194	2.82	0.00396	0.638
E	0.455	0.0295	0.421	0.00390	0.310

co-rotating digital video camera attached to the turntable and positioned to view vertically down into the cylinder's interior (see Figure 1). At the end of each experiment, the velocity data were generated from the captured images using standard PIV software. Additional qualitative insight into the relative flow was obtained from the captured images by generating images of the flow streamlines. This was achieved by recording streak paths (or time exposures) of the tracer particles over durations of between 15 and 30 s. Here we use these streak line images to illustrate the flow's key features.

B. Observations

The flow features reported here for the sliced square cylinder are, in a number of ways, similar to those reported previously for a uniform-depth square cylinder.[14] However, notable differences were observed (a) in the region immediately above the inclined base, and (b) for the case of relatively small Burger number (e.g., in experiment E, where $S = 0.421$). Hence, in this section we use streak line images from experiment C (Figure 2) to illustrate the key features observed in the flow's bulk interior

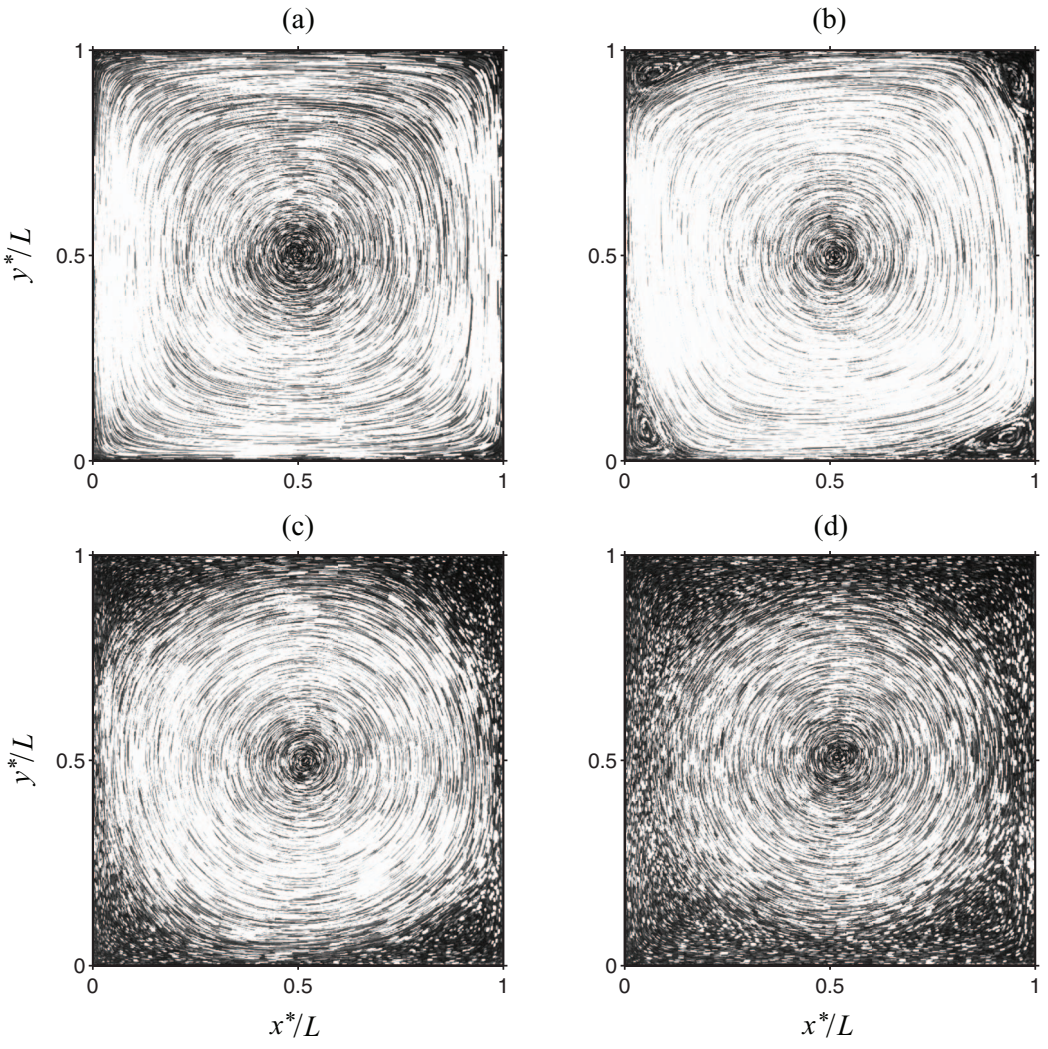

FIG. 2. Experiment C ($\Omega = 0.429$ rad/s, $\epsilon = 0.0254$, $S = 4.46$, $z_0/H = 0.329$): (a)–(d) show streak line images taken, respectively, at times $\epsilon\Omega t^* = 0.22$, 1.3, 16, and 26 (or, $E^{1/2}\Omega t^* = 0.034$, 0.21, 2.6, and 4.1). The base slope is in the x^*-direction, with $x^*/L = 0$ and $x^*/L = 1$ corresponding, respectively, to the bottom and top of the slope (see Figure 1). The exposure duration in (a) was 15 s, and in (b)–(d) was 30 s.

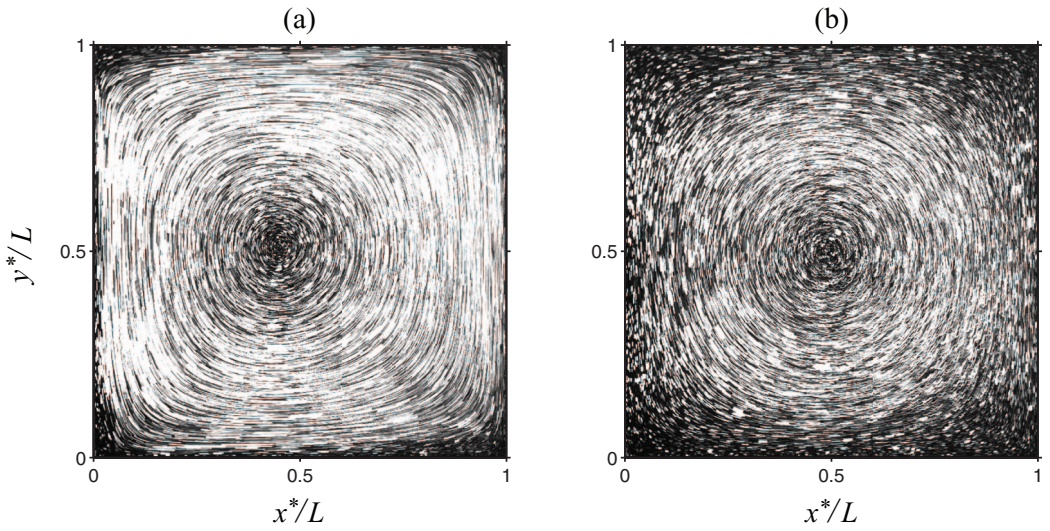

FIG. 3. Experiment A ($\Omega = 0.209$ rad/s, $\epsilon = 0.0521$, $S = 15.4$, $z_0/H = 0.144$): (a) and (b) show streak line images taken, respectively, at times $\epsilon\Omega t^* = 0.65$ and 33 (or, $E^{1/2}\Omega t^* = 0.072$ and 3.6). The base slope is in the x^*-direction, with $x^*/L = 0$ corresponding to the bottom of the slope (see Figure 1). The exposure duration in (a) was 15 s, and in (b) was 30 s.

when $S \geqslant \mathcal{O}(1)$, which are similar to those reported for the uniform-depth square cylinder, and are repeated here for completeness. Streak line images from experiment A (Figure 3) and experiment E (Figure 4) will then be used to illustrate, respectively, the differences observed in the near-base region and at relatively small S.

Figure 2 shows a selection of streak line images from experiment C, taken at various times (see caption for details). The impulsive increase of the cylinder's rotation rate gives rise to a starting flow, which relative to the co-rotating reference frame takes the form of a single anticyclonic cell, with its axis coincident with the central vertical axis of the cylinder (i.e., the rotation axis), and with closed streamlines that fill the interior domain. The structure of this starting flow can be seen clearly in Figure 2(a), where recalling the cyclonic direction is clockwise. At early times, which are

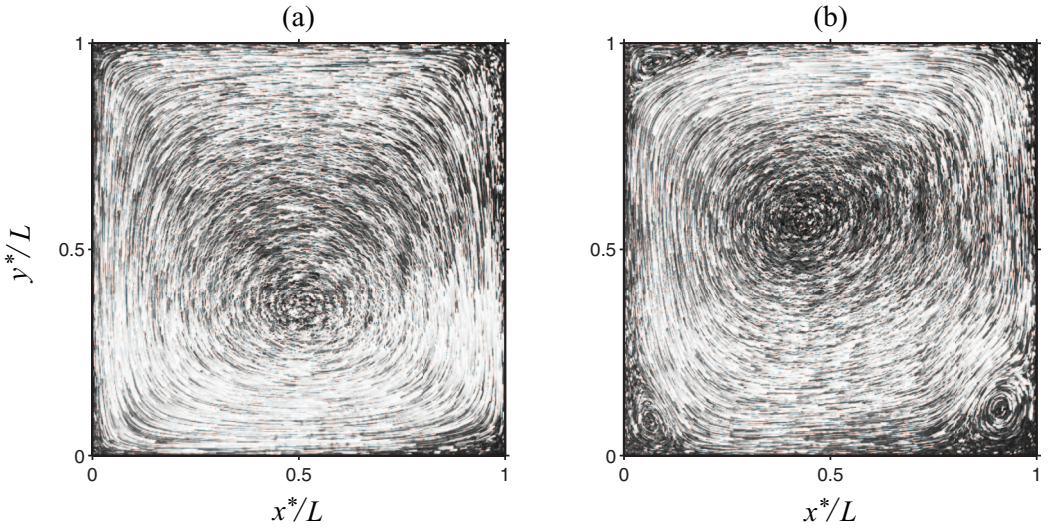

FIG. 4. Experiment E ($\Omega = 0.455$ rad/s, $\epsilon = 0.0295$, $S = 0.421$, $z_0/H = 0.310$): (a) and (b) show streak line images taken, respectively, at times $\epsilon\Omega t^* = 0.34$ and 1.9 (or, $\alpha\Omega t^* = 2.01$ and 11.3). The base slope is in the x^*-direction, with $x^*/L = 0$ corresponding to the bottom of the slope (see Figure 1). In both cases the exposure duration was 17 s.

small compared to $\epsilon^{-1}\Omega^{-1}$, the sidewall boundary layers are still forming and remain attached, and so have had no noticeable influence on the interior flow. Also, the Ekman layers are not yet fully formed at times small compared to $E^{-1/2}\Omega^{-1}$, so there is no vertical motion within the fluid's interior at early times. Hence, during this initial period, the anticyclonic starting flow within the bulk interior is effectively inviscid and two-dimensional.[12,14]

During the second stage the Ekman layers and sidewall boundary layers are fully established. The most noticeable feature during this stage is caused by the separation and detachment of the sidewall boundary layers in the upstream region of the cylinder's corners, which results in the formation of four corner cells, each consisting of a vertical, cyclonic line vortex which extends over the tank depth. The first evidence of the corner cells is observed in the streak line images after three or four rotation periods, and Figure 2(b) shows that the corner cells are clearly formed at time $\epsilon\Omega t^* \approx 1$. The length of the streak lines shows that the relative motion in the corner cells is weak compared to that observed in the main cell (the peak flow speed in the corner cells was typically less than 20% of that in the main cell).[14] Each corner cell grows in cross-section as more cyclonic vorticity is advected into these regions. This results in the detachment point upstream of a corner moving upstream, back along the sidewall, and the reattachment point downstream of a corner moving further downstream, along the adjacent sidewall. Notably, here, for a cylinder with a square cross-section and small base slope, the four corner cells grow at the same rate, in contrast with what is observed in a rectangular tank (either with a flat or inclined base), where the corner cells form in an asymmetric way, with larger cells developing downstream of the long sides and small cells downstream of the short sides.[12,13]

The growth of the cyclonic corner cells slows as the detachment and reattachment points on each sidewall move closer together, as this reduces the surface area on the sidewall adjacent to which the cyclonic vorticity is produced. Eventually, during the final stage, a quasi-steady state is reached when the deformed perimeter of the main cell is circular and the fluid in the corner regions is essentially spun-down, as shown in Figure 2(c). For subsequent times this basic flow pattern persists as the relative flow of the main, anticyclonic cell is gradually spun-up on the $E^{-1/2}\Omega^{-1}$ time scale. Figure 2(d) shows the relative decay of motion with the main cell after four spin-up time scales.

The streak line images in Figure 3 are from experiment A, and correspond to height $z_0/H = 0.144$ above the mid-slope level. By comparing Figure 3(a) with Figure 2(a) we see how the starting-flow's structure is affected in the region close to the base slope. That is, within the bulk interior the cell is symmetric (see Figure 2(a)) with its central axis coincident with the rotation axis ($x^*/L = 0.5$, $y^*/L = 0.5$), and this remains the case throughout the experiment's duration. However, in the near-base region the starting-flow cell is positioned centrally only at very early times, but then quickly becomes asymmetric (as in Figure 3(a)), with a small but noticeable shift of the cell's axis towards the deeper side of the cylinder (at $x^*/L = 0$), but throughout being positioned centrally with respect to the cross-slope y-direction. This effect – the down-slope shift of anticyclones over topography – has been reported previously in relation to β-plane effects,[17] and was observed by van Heijst *et al.*[13] in their experiments on spin-up in an inclined-base rectangular tank. Moreover, this effect in the starting flow was modelled by van Heijst *et al.*,[13] by applying conservation of vorticity, but with standard shallow-water assumptions and a two-dimensional transport streamfunction to incorporate the base-slope condition.[18] For the case when the slope height is small compared to the fluid's depth, it was also shown that this effect is bottom-trapped,[13] as was certainly the case in our experiments (where $H/L\tan\alpha = 0.138$), with no evidence of this down-slope asymmetry in the starting flow observed at heights $z^*/H \gtrsim 0.2$. Note that, as the flow evolves on the longer time scale and spins up, the centre of cell in this near-base region gradually drifts towards, and eventually becomes realigned with the central axis of the cylinder, as shown by the streak line image in Figure 3(b), which corresponds to time $E^{1/2}\Omega t^* = 3.6$.

We now consider the small-S case and the two streak line images in Figure 4, which are from experiment E ($S = 0.421$, $z_0/H = 0.310$). Once again, the starting-flow's structure at early times was symmetric, with its axis positioned centrally and aligned with the rotation axis. However, at time $\alpha\Omega t^* \approx 1$, wave-like motions had developed, causing the vertical axis of the cell to oscillate about the cylinder's central axis, with components in the cross-slope y-direction and, to a lesser extent, in the along-slope x-direction. (Note, this type of wave motion was not detected in any of

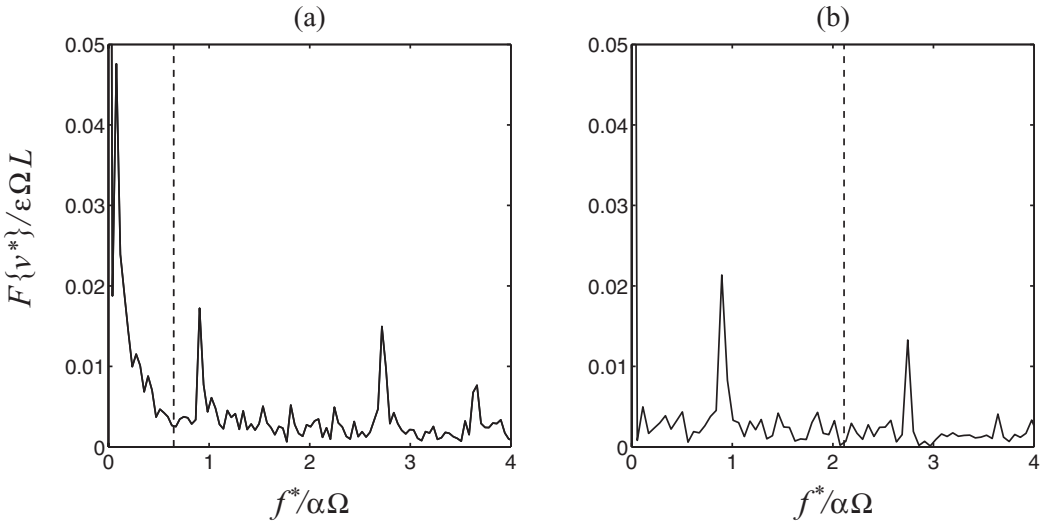

FIG. 5. Plots showing FFTs (denoted $F\{\ \cdot\ \}$) of time series of the measured velocity component v^* (at the interior point $x^*/L = 0.2$, $y^*/L = 0.5$). Plot (a) shows data from experiment E ($\epsilon = 0.0295$, $S = 0.421$, $z_0/H = 0.310$); plot (b) shows data from experiment C ($\epsilon = 0.0254$, $S = 4.46$, $z_0/H = 0.329$). In each case, v^* and the frequency f^* (in Hz) have been made dimensionless by $\epsilon\Omega L$ and $\alpha\Omega$. The broken lines show $f^*/\alpha\Omega = \sqrt{S}$, the upper bound for the Rossby-wave frequencies.

the other experiments listed in Table I.) The peak amplitude of the cross-slope oscillation, which can be seen by comparing the two images in Figure 4, was $\approx 0.25L$: The corresponding oscillation period was $\approx 20(\alpha\Omega)^{-1}$. Notably, these wave motions were damped relatively quickly, and were no longer discernible in the streak line images for times $\alpha\Omega t^* \gtrsim 35$, after which the vertical axis of the main cell remained essentially stationary and more or less realigned with the cylinder's central axis. The flow's evolution at subsequent times was then very similar to the flow described above for the $S \geqslant \mathcal{O}(1)$ cases.

Further insight into the nature of these damped wave motions can be obtained from the spectral properties of the measured velocity data. The plots in Figure 5 show FFTs obtained from time-series measurements of the velocity component v^*, sampled at the interior point $x^*/L = 0.2$, $y^*/L = 0.5$, and plotted against frequency f^*. (In both plots, v^* and f^* have been non-dimensionlised by $\epsilon\Omega L$ and $\alpha\Omega$.) The data in Figure 5(a) are from experiment E ($S = 0.421$). For comparison, the data in Figure 5(b) are from experiment C ($S = 4.46$), where no evidence of these waves was detected (see Figure 2). [The other key parameters (Ω, ϵ, z_0/H) for these two experiments are comparable.] First note that, in Figure 5, both of the FFTs show contributions at $f^*/\alpha\Omega \approx 0.9$ and 2.8: We emphasize here that these contributions do not correspond to wave motions of the type evident in Figure 4, but to small-amplitude oscillations (present in all five experiments) that were a facet of the set-up procedure, induced as the fluid was incrementally spun-up from rest to the initial rotation rate $\Omega - \Delta\Omega$. (These small-amplitude oscillations were also present in u^*-component velocity data.) We found that even on the long diffusive time scale $E^{-1}\Omega^{-1}$ ($\approx$40 h), these small oscillatory motions were still present and, most importantly, only slightly attenuated over this period. It was clear, however, they had little affect on the dynamics of the spin-up process on the $E^{-1/2}\Omega^{-1}$ time scale, and so these components can henceforth be ignored.

The wave motions observed in experiment E correspond – in Figure 5(a) – to the FFT contributions at frequencies $0 < f^*/\alpha\Omega \lesssim 0.6$. The asymptotic analysis reported in Sec. III indicates the presence of Rossby modes with frequencies $0 < f^*/\alpha\Omega \leqslant \sqrt{S}$: The broken lines in Figure 5 have been included to indicate the upper limit of this range (see caption), and show that the FFT contributions at the lower frequencies in Figure 5(a) do appear to be a manifestation of those modes. Likewise, in Figure 5(b), where the data are taken from experiment C ($S = 4.46$), where there was no evidence of these wave motions, there are no (relevant) FFT contributions corresponding to Rossby modes. The theory in Sec. III also shows the fluid's background density stratification

significantly damps these Rossby modes, and that the magnitude of this damping increases with S. The experimental data show that for $S \gtrsim \mathcal{O}(1)$ the damping is severe enough to completely suppress these Rossby modes, and it is only at small S that they are evident. We shall return to discuss this further when we introduce the relevant theory in Sec. III F 2.

III. LINEAR THEORY

Restrictions on the analysis derived and presented in this section have been stated in (2) and (4), which are assumed to hold throughout.

A. Formulation

The flow configuration has been described above and is shown in Figure 1. We use the Boussinesq equations, neglecting any modification of apparent gravity due to centrifugal force, and write the Navier-Stokes equations in the reference frame of the new rotation rate. Let the dimensional density ($\overline{\rho}^*$) and pressure ($\overline{p}^*$) be written in this system as

$$\overline{\rho}^*(\mathbf{x}^*, t^*) = \rho_\ell + \rho_s^*(z^*) + \rho^*(\mathbf{x}^*, t^*), \tag{5a}$$

$$\overline{p}^*(\mathbf{x}^*, t^*) = p_s^*(z^*) + p^*(\mathbf{x}^*, t^*), \tag{5b}$$

where ρ_s^* and p_s^* are the contributions associated with the background stratification, ρ_ℓ is a constant reference density (taken here to be the initial density at the container's lid), and ρ^* and p^* are the perturbations arising due to the increase in rotation rate of the cylinder. It is assumed throughout that $\rho^* \ll \rho_s^*,\ \rho_\ell$. We now put all of the flow variables in dimensionless form as

$$\mathbf{u} = \frac{\mathbf{u}^*}{\epsilon\Omega L}, \mathbf{x} = \frac{\mathbf{x}^*}{L}, t = \Omega t^*, \rho = \frac{g\rho^*}{\epsilon\rho_\ell\Omega^2 L}, p = \frac{p^*}{\epsilon\rho_\ell\Omega^2 L^2}, \tag{6}$$

where the velocity vector $\mathbf{u}(\mathbf{x}, t)$ has components (u, v, w). Then, the dimensionless form of the Boussinesq equations is

$$\nabla \cdot \mathbf{u} = 0, \tag{7a}$$

$$\mathbf{u}_t + \epsilon(\mathbf{u} \cdot \nabla)\mathbf{u} + 2(\hat{\mathbf{z}} \times \mathbf{u}) + \rho\hat{\mathbf{z}} + \nabla p = E\nabla^2\mathbf{u}, \tag{7b}$$

$$\rho_t + \epsilon(\mathbf{u} \cdot \nabla)\rho - Sw = (E/Sc)\nabla^2\rho, \tag{7c}$$

where the Rossby, Ekman, Burger, and Schmidt numbers have been previously defined, but are given here again for convenience:

$$\epsilon = \frac{\Delta\Omega}{\Omega}, \quad E = \frac{\nu}{\Omega L^2}, \quad S = \left(\frac{N}{\Omega}\right)^2, \quad Sc = \frac{\nu}{\kappa}. \tag{8}$$

In this work, we assume that the buoyancy frequency N remains constant throughout. The corresponding initial and boundary conditions are then

$$\mathbf{u} = \hat{\mathbf{z}} \times (\mathbf{x} - \mathbf{x}_0) = \left(\tfrac{1}{2} - y, x - \tfrac{1}{2}, 0\right), \rho = 0 \text{ for } t = 0, \mathbf{x} \in \mathcal{D}, \tag{9a}$$

$$\mathbf{u} = 0, \frac{\partial\rho}{\partial n} = 0 \text{ for } \mathbf{x} \in \partial\mathcal{D}, t > 0, \tag{9b}$$

where $\mathbf{x}_0 = (1/2, 1/2, 0)$, $\mathcal{D} = \{(x, y, z) : x, y \in [0, 1] \text{ and } (x - 1/2)\tan\alpha \leqslant z \leqslant h\}$ is the flow domain, $\partial\mathcal{D}$ the domain boundary, and n is the normal direction at each boundary. For convenience in what comes below, let $\partial\mathcal{D}_v$ denote that portion of $\partial\mathcal{D}$ that are the four vertical walls. In what follows, we take α be small, so $\tan\alpha \approx \alpha$.

B. Overview of the analysis

Before proceeding to the details of the asymptotic analysis, in all of its algebraic complexity, we summarize here the basic ideas. Following the increase in the container's rotation rate, for time scales that are long compared to the rotation period but short compared to wave-propagation and spin-up times, there is an impulsive starting flow which takes the form of a large, central anticyclone (see Figure 2(a)), with thin Rayleigh layers on the vertical sidewalls. On this time scale no vertical motion has yet occurred. Within the bulk interior this starting flow is essentially inviscid and can be described by a simple two-dimensional Laplace equation (see Sec. III C 1), using the approach reported previously in Foster and Munro.[14]

In Sec. III D we formulate the inviscid, interior motion on a time scale of order α^{-1}, which gives rise to Rossby waves, and the subsequent decay of motion on the longer $E^{-1/2}$ time scale by means of Ekman friction on the top and bottom boundaries. Based on the understandings of Walin,[5] we know that, on the α^{-1} time scale, there is no inflow into the Ekman layers; that inflow occurs in regions near the junction of horizontal and vertical walls—in regions of width $E^{1/2}/\alpha$. However, unlike the axisymmetric case, the fluid entering each Ekman layer in these small regions flows further into the corner, and then erupts over a much smaller scale, of width $E^{1/2}$. What occurs, then, are recirculating corner eddies of dimension $E^{1/2}/\alpha$, with axes that are parallel to the base-sidewall (or lid-sidewall) intersections. As in the case of the uniform-depth square cylinder described in Foster and Munro,[14] the $E^{1/2}/\alpha$-scale corner eddies now grow to fill the container on the $E^{-1/2}$ time scale, so that fluid flows from the interior core and into the Ekman layers, flows on into the corners, and then singularly erupts into the interior. These corner eruptions are crucial to the dynamics of the interior motion, and set these asymmetric spin-up problems apart from axisymmetric spin-up, as noted above.

The remaining sections are arranged as follows. In Sec. III C, we formulate the core flow and provide a brief examination of the early-time motion in Sec. III C 1. The construction of the system of differential equations that describes the interior flow may be found in Sec. III D. The solution is obtained in the following two sections: In Sec. III E, the $E^{1/2}t \to \infty$ limit of the interior motion is found, attaining that limiting form after the transient motion described in Sec. III F has decayed away. Finally, in Sec. V we analyze the vertical-wall boundary layers on the horizontal, tangential velocity component, which slips over the wall in all of the foregoing analysis. Finite-time vorticity eruption from those boundary layers is responsible for the formation of the cyclonic corner eddies described in Sec. II.

C. The inviscid interior flow

We now perform the "outer limit" for $0 < E, \epsilon \ll 1$. Ignoring terms of order E and ϵ in Eq. (7) gives

$$\nabla \cdot \mathbf{u} = 0, \tag{10a}$$

$$\mathbf{u}_t + 2(\hat{\mathbf{z}} \times \mathbf{u}) + \rho\hat{\mathbf{z}} + \nabla p = 0, \tag{10b}$$

$$\rho_t - Sw = 0. \tag{10c}$$

Forming an equation for the vertical vorticity component, one may then eliminate the vertical velocity and density perturbation, and that leads to a single equation for the pressure,[14] namely,

$$\frac{\partial^3}{\partial t^3}\left(\nabla^2 p\right) + \frac{\partial}{\partial t}\left(S\nabla_1^2 p + 4p_{zz}\right) = 0, \tag{11}$$

where in the second term $\nabla_1^2 \equiv \partial^2/\partial x^2 + \partial^2/\partial y^2$ is the horizontal Laplacian. The relation of the velocity components to the pressure is

$$u_{tt} + 4u + p_{xt} + 2p_y = 0, \quad v_{tt} + 4v + p_{yt} - 2p_x = 0, \quad w_{tt} + Sw + p_{zt} = 0. \tag{12}$$

The boundary conditions on the top and bottom walls are no-penetration. The unit vector normal to the inclined base plane is $\hat{\mathbf{n}} = \cos\alpha\hat{\mathbf{z}} - \sin\alpha\hat{\mathbf{x}}$, and so the no-penetration condition ($\mathbf{u} \cdot \hat{\mathbf{n}} = 0$),

noting that α is small, gives

$$w - \alpha u = 0. \tag{13}$$

The general initial-value problem is exceedingly complicated, not only because of this boundary condition, but also because of the boundary conditions at the vertical walls, deduced from (12), that involve normal and tangential derivatives at those walls – making the problem non-separable. So here, we examine relatively long time scales. Proceeding, then, on that basis, for any time scale shorter than α^{-1}, allowing the neglect of the αu term, we have

$$p_{zt} = 0 \text{ at } z = 0, h, \text{ for } t = o(\alpha^{-1}). \tag{14}$$

The lateral walls conditions are more complicated. For example, on $x = 0$, no penetration means that

$$p_{xt} + 2p_y = 0. \tag{15}$$

If the time is very short, we get $p_x = 0$, and so, in general,

$$p_n \text{ is constant on } \partial\mathcal{D}_v, \text{ for } t \ll 1. \tag{16}$$

If $t \gg 1$ but smaller than α^{-1}, the other term dominates, and so we get

$$p = 0 \text{ on } \partial\mathcal{D}_v, \text{ for } 1 \ll t \ll \alpha^{-1}. \tag{17}$$

The partial differential equation (11) is valid for all times short of the diffusive time scale.

1. The inviscid, two-dimensional starting flow

The analysis here is virtually identical to that reported previously for the uniform-depth square cylinder.[14] Here, as there, since $\nabla_1^2 p_t = \nabla_1^2 p_{tt} = 0$ at $t = 0$, using z-independence as guaranteed by (14), Eq. (11) reduces to

$$\nabla_1^2 p = 4. \tag{18}$$

For times $t \ll 1$ the relevant boundary condition is (16), and the solution to Eq. (18) is simply the initial, rigid rotation, so nothing happens on this scale. For times $t = \mathcal{O}(1)$, the boundary conditions are mixed, as indicated by (12). For $1 \ll t \ll \alpha^{-1}$ the condition (17) leads to a double Fourier sine series. That solution is[14]

$$p = -\sum_{m=1}^{\infty}\sum_{n=1}^{\infty} \frac{4\gamma_{mn}}{(m^2+n^2)\pi^2}\phi_m(x)\phi_n(y), \tag{19}$$

where for convenience we define

$$\phi_k(x) \equiv \sin(k\pi x), \quad \gamma_{mn} = q_m q_n, \quad q_n = \frac{2\,[1-(-1)^n]}{n\pi}. \tag{20}$$

From this solution, with reference to (12), the velocity components, for all $1 \ll t \ll \alpha^{-1}$, are given by

$$u = -\frac{p_y}{2}, \quad v = \frac{p_x}{2}. \tag{21}$$

This same sort of solution for early times has been seen in a variety of contexts by other investigators.[11–13]

At early times, and at heights above the near-base region, the experimental data were found to exhibit excellent agreement with the streamfunction (19) and the corresponding velocity components defined by (21). Figure 6(a) shows a sample of streamlines from (19) compared with the streak line image already shown in Figure 2(a), from experiment C (at $t = \Omega t^* = 8.7$ and $z_0/H = 0.329$). Figure 6(b) shows measurements, also from experiment C, of the horizontal velocity component, v, extracted along the symmetry axis $y = 1/2$, plotted against x, and compared with the corresponding theoretical velocity profile defined using (19) and (21).

Finally, we note here that the early time streamfunction defined in (19) provides the initial condition for the motion on the time scale $t \sim \alpha^{-1}$ considered in Subsection III D.

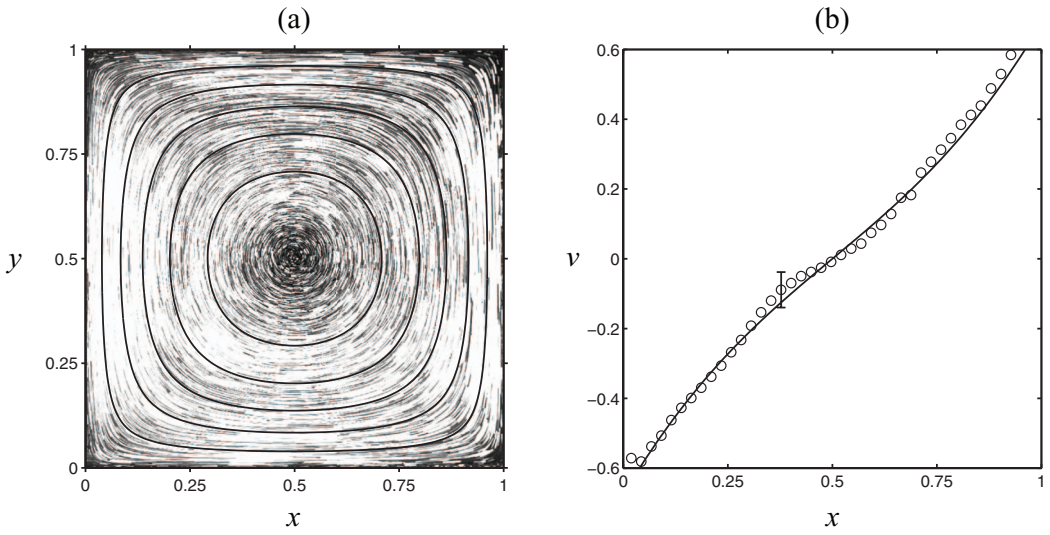

FIG. 6. (a) The solid lines show contours of the streamfunction (19), superimposed on top of the streak line image shown previously in Figure 2(a) (from experiment C, at dimensionless time $t = \Omega t^* = 8.7$). (b) The solid line shows the velocity component $v = p_x/2$ along the symmetry axis $y = 1/2$, obtained using Eqs. (19) and (21), plotted against x, and compared with corresponding measured velocity data taken from experiment K (○) at time $t = 4.4$. The measured velocity profile shown is an average of data taken over a 1 s period, and the error bar shown is representative of the peak variability observed over this duration.

D. Formulation of the motion on the α^{-1} and $E^{-1/2}$ time scales

The full boundary condition on the lower wall, transferred to $z = 0$, includes the standard formula for outflow from the Ekman layer, and is

$$w - \alpha u = \frac{E^{1/2}}{2}\left(v_x - u_y\right) + \mathcal{O}\left(\alpha^2\right). \tag{22}$$

For $t > \mathcal{O}(1)$, Eq. (12) requires that the vertical velocity is given by

$$w = -\frac{1}{S}\, p_{zt},$$

and since p is a streamfunction for the horizontal motion according to (21), boundary condition (22) becomes

$$p_{zt} = \frac{\alpha S}{2} p_y - \frac{S E^{1/2}}{4}\nabla_1^2 p.$$

This equation suggests that a time scale of order α^{-1} is relevant, and so we introduce

$$\tau = \alpha t, \quad \eta = E^{1/2}/\alpha, \tag{23}$$

and then the boundary condition becomes

$$p_{z\tau} = \frac{S}{2} p_y - \eta\frac{S}{4}\nabla_1^2 p \ \text{ on } z = 0, \tag{24}$$

where $\eta = o(1)$. The quantity η is actually the ratio of the Rossby-wave frequency to the spin-up time scale. The corresponding boundary condition at the upper, flat boundary is

$$p_{z\tau} = \eta\frac{S}{4}\nabla_1^2 p \text{ on } z = h. \tag{25}$$

Before proceeding, note that balancing the left- and right-hand-side terms in (24) and (25) leads to the η scale for Ekman inflow – in the corners – as discussed briefly in Sec. III B.

We now expand the solution in the interior as an asymptotic series,

$$p(\mathbf{x}, \tau) = p_0(\mathbf{x}, \tau) + \eta p_1(\mathbf{x}, \tau) + \ldots, \tag{26}$$

and substitute into (11), with the time suitably scaled. The result for the first-order problem is the equation

$$\nabla_1^2 p_0 + \frac{4}{S} p_{0zz} = 4, \tag{27}$$

subject to no penetration at the vertical walls, and

$$p_{0z\tau} = \frac{S}{2} p_{0y} \text{ on } z = 0, \quad p_{0z\tau} = 0 \text{ on } z = h. \tag{28}$$

Before turning to the details of the solution, we note that if one looks for plane-wave solutions of the homogeneous version of (27) in the form

$$\exp(ik_1 x + ik_2 y + i\omega\tau)\cosh[a(z-h)],$$

which automatically satisfies the upper boundary condition, we obtain, on using the $z = 0$ boundary condition from (28), the dispersion relation

$$\omega = -\frac{S}{2} k_2 \frac{\coth(ah)}{a}, \quad a = \frac{1}{2}\sqrt{S(k_1^2 + k_2^2)}. \tag{29}$$

This result is well-known, and is included here for completeness only: For example, compare (29) with Eq. (2.5) on p. 284 of Rhines' paper on waves in a rotating, stratified container.[19] The result also goes to the proper homogeneous dispersion relation for Rossby waves in the limit $S \to 0$. Clearly, each of these waves propagates across the slope, like their homogeneous counterparts,[10] but here, of course, there is z-dependence due to the stratification. In Sec. III F, we determine the Rossby-wave spectrum for this geometry, with the side-wall conditions determining the possible frequencies. Note that the frequencies and hence the wave speeds (for these simple plane waves, and also for the geometry at hand) are monotone in S, scaling with $\sqrt{S}$ for sufficiently large S.

A curious thing happens here: Note that integration of boundary condition (28) over the bottom wall, for $0 \le x \le 1$ and $0 \le y \le 1$, gives

$$\int_0^1 \int_0^1 p_{0z\tau}\, \mathrm{d}x\, \mathrm{d}y = 0, \tag{30}$$

using the sidewall condition on p_0. This same zero average occurs on $z = h$. Physically, this condition means there is no net inflow into the Ekman layers on either top or bottom boundary, and that is possible only with Ekman eruptions in the corners. Hence, any proper solution of this boundary-value problem must satisfy this average condition. It appears that double Fourier series solution to (27) is not adequate to the satisfaction of this averaged condition, since such a series inherently has a non-zero average in x-y, a result that determines the approach used below.

This problem seems amenable to multi-variable expansion techniques, but the slow-time effects are quite complicated, so we proceed by working with the full equations written to order η, and then carefully taking the limit $\eta \to 0$ when most convenient. What is particularly surprising here is that there seem to be two rather different sorts of interior motion: There are stratified Rossby waves damped by the Ekman suction effects (which are analyzed in Sec. III F 2), and then there are additional unsteady non-wave-like modes that decay on the α^{-1} timescale (see Sec. III F 1).

In an *ansatz* like that employed previously for the uniform-depth cylinder,[14] we write

$$p(\mathbf{x}, \tau) = P(\mathbf{x}, \tau) + K_1(x, y, \tau) + zK_2(\tau) + z^2 K_3(\tau), \tag{31a}$$

$$P(\mathbf{x}, \tau) \equiv \sum_{m=1}^{\infty} \sum_{n=1}^{\infty} A_{mn}(z, \tau)\phi_m(x)\phi_n(y). \tag{31b}$$

The appropriate sidewall boundary conditions are that, at a fixed height and time, the pressure $p(\mathbf{x}, \tau)$ is constant along the sidewall, and from (31a) that constant is $zK_2 + z^2 K_3$. Substitution of (31) into

(27) shows that

$$\frac{4}{S}\frac{\partial^2 A_{mn}}{\partial z^2} - \pi^2(m^2+n^2)A_{mn} = 4\gamma_{mn}, \tag{32}$$

which has solution

$$A_{mn} = C_{mn}(\tau)\cosh[\mu_{mn}(z-h)] + D_{mn}(\tau)\sinh[\mu_{mn}(z-h)] - \frac{S\gamma_{mn}}{\mu_{mn}^2}, \tag{33}$$

where

$$\mu_{mn}^2 \equiv \frac{S(m^2+n^2)\pi^2}{4}. \tag{34}$$

Further, K_1 satisfies

$$\nabla_1^2 K_1 = -\frac{8K_3}{S}, \tag{35}$$

so that

$$K_1 = 2K_3\sum_{m=1}^{\infty}\sum_{n=1}^{\infty}\frac{\gamma_{mn}}{\mu_{mn}^2}\phi_m(x)\phi_n(y), \tag{36}$$

where γ_{mn} and ϕ_m have been defined in (20).

Substituting into the upper boundary condition in (25) gives

$$K_{2\tau} + 2hK_{3\tau} + \sum_{m=1}^{\infty}\sum_{n=1}^{\infty}\mu_{mn}D_{mn\tau}\phi_m(x)\phi_n(y) = -\eta\sum_{m=1}^{\infty}\sum_{n=1}^{\infty}\mu_{mn}^2\left(C_{mn} - \frac{S\gamma_{mn}}{\mu_{mn}^2}\right)\phi_m(x)\phi_n(y) - 2\eta K_3 + \mathcal{E}_h. \tag{37}$$

Recall that we must account for the singular eruptions of the Ekman fluid, so $\mathcal{E}_h$ denotes the singular eruptions at the boundaries of the container's lid, as indicated in Equation (30). When integrated over $0 \le x \le 1$, $0 \le y \le 1$, we require that $\mathcal{E}_h$ cancels all Ekman outflow along the surface. Thus,

$$\frac{1}{4}\sum_{m=1}^{\infty}\sum_{n=1}^{\infty}\mu_{mn}D_{mn\tau}\gamma_{mn} + K_{2\tau} + 2hK_{3\tau} = 0. \tag{38}$$

Subtracting (38) from (37) leads to

$$\sum_{m=1}^{\infty}\sum_{n=1}^{\infty}\mu_{mn}D_{mn\tau}\left[\phi_m(x)\phi_n(y) - \frac{1}{4}\gamma_{mn}\right] = -\eta\sum_{m=1}^{\infty}\sum_{n=1}^{\infty}\mu_{mn}^2\left(C_{mn} - \frac{S\gamma_{mn}}{\mu_{mn}^2}\right)\phi_m(x)\phi_n(y) - \eta 2K_3 + \mathcal{E}_h. \tag{39}$$

We now turn to the bottom boundary condition in (24), which becomes

$$K_{2\tau}+\sum_{m=1}^{\infty}\sum_{n=1}^{\infty}\mu_{mn}\left[D_{mn\tau}\cosh(\mu_{mn}h)-C_{mn\tau}\sinh(\mu_{mn}h)\right]\phi_m(x)\phi_n(y)$$
$$=\frac{S}{2}\sum_{m=1}^{\infty}\sum_{n=1}^{\infty}\left[(2K_3-S)\frac{\gamma_{mn}}{\mu_{mn}^2}+C_{mn}\cosh(\mu_{mn}h)-D_{mn}\sinh(\mu_{mn}h)\right]n\pi\phi_m(x)\zeta_n(y)$$
$$+\eta\sum_{m=1}^{\infty}\sum_{n=1}^{\infty}\mu_{mn}^2\left[C_{mn}\cosh(\mu_{mn}h)-D_{mn}\sinh(\mu_{mn}h)-\frac{S\gamma_{mn}}{\mu_{mn}^2}\right]\phi_m(x)\phi_n(y)$$
$$+2\eta K_3+\mathcal{E}_0, \quad (40)$$

where $\mathcal{E}_0$ denotes the singular eruptions at the base. On integrating over $0\le x\le 1$, $0\le y\le 1$ as above, we obtain the result

$$K_{2\tau}+\frac{1}{4}\sum_{m=1}^{\infty}\sum_{n=1}^{\infty}\mu_{mn}\gamma_{mn}\left[D_{mn\tau}\cosh(\mu_{mn}h)-C_{mn\tau}\sinh(\mu_{mn}h)\right]=0. \quad (41)$$

On subtracting (41) from (40), we obtain the result

$$\sum_{m=1}^{\infty}\sum_{n=1}^{\infty}\mu_{mn}\left[D_{mn\tau}\cosh(\mu_{mn}h)-C_{mn\tau}\sinh(\mu_{mn}h)\right]\left[\phi_m(x)\phi_n(y)-\frac{1}{4}\gamma_{mn}\right]$$
$$=\frac{S}{2}\sum_{m=1}^{\infty}\sum_{n=1}^{\infty}\left[C_{mn}\cosh(\mu_{mn}h)-D_{mn}\sinh(\mu_{mn}h)+(2K_3-S)\frac{\gamma_{mn}}{\mu_{mn}^2}\right]n\pi\phi_m(x)\zeta_n(y)$$
$$+\eta\sum_{m=1}^{\infty}\sum_{n=1}^{\infty}\mu_{mn}^2\left[C_{mn}\cosh(\mu_{mn}h)-D_{mn}\sinh(\mu_{mn}h)-\frac{S\gamma_{mn}}{\mu_{mn}^2}\right]\phi_m(x)\phi_n(y)$$
$$+2\eta K_3+\mathcal{E}_0. \quad (42)$$

Combining the averaged equations (38) and (41), one obtains an equation for K_3 which may easily be integrated, and on using homogeneous initial conditions for C_{mn} and D_{mn}, we have

$$2hK_3+\frac{1}{4}\sum_{m=1}^{\infty}\sum_{n=1}^{\infty}\mu_{mn}\gamma_{mn}\left\{D_{mn}[1-\cosh(\mu_{mn}h)]+C_{mn}\sinh(\mu_{mn}h)\right\}=0. \quad (43)$$

Using the orthogonality of the basis functions $\phi_m(x)$ and $\phi_n(y)$, (39) and (42) become the differential equations for the Fourier coefficients, which are

$$\mu_{mk}D_{mk\tau}-\frac{1}{4}\gamma_{mk}\sum_{r=1}^{\infty}\sum_{s=1}^{\infty}\mu_{rs}\gamma_{rs}D_{rs\tau}=-\eta\gamma_{mk}(2K_3-S)-\eta\mu_{mk}^2C_{mk}, \quad (44a)$$

$$\mu_{mk}D_{mk\tau}\cosh(\mu_{mk}h)-\mu_{mk}C_{mk\tau}\sinh(\mu_{mk}h)$$
$$-\frac{1}{4}\gamma_{mk}\sum_{r=1}^{\infty}\sum_{s=1}^{\infty}\gamma_{rs}\mu_{rs}\left[D_{rs\tau}\cosh(\mu_{rs}h)-C_{rs\tau}\sinh(\mu_{rs}h)\right]$$
$$=S\sum_{n=1}^{\infty}g_{kn}\left[(2K_3-S)\frac{\gamma_{mn}}{\mu_{mn}^2}+C_{mn}\cosh(\mu_{mn}h)-D_{mn}\sinh(\mu_{mn}h)\right]$$
$$+\eta\mu_{mk}^2C_{mk}\cosh(\mu_{mk}h)-\eta\mu_{mk}^2D_{mk}\sinh(\mu_{mk}h)$$
$$+\eta\gamma_{mk}(2K_3-S), \quad (44b)$$

where

$$g_{kn} = \begin{cases} 0, & n = k \\ \dfrac{nk}{k^2 - n^2}\left[1 - (-1)^n(-1)^k\right], & n \neq k \end{cases}. \tag{45}$$

Now, we split the solution, in conventional fashion, into homogeneous and particular components,

$$C_{mn}(\tau) = c_{mn}(\tau) + \mathcal{C}_{mn}, \tag{46a}$$

$$D_{mn}(\tau) = d_{mn}(\tau) + \mathcal{D}_{mn}, \tag{46b}$$

$$K_i(\tau) = k_i(\tau) + \mathcal{K}_i \quad i = 1, 2, 3, \tag{46c}$$

the latter components $\mathcal{C}_{mn}$, $\mathcal{D}_{mn}$, and $\mathcal{K}_i$ corresponding to the steady state.

E. Steady-state solution

By direct substitution of Eqs. (46a)–(46c) into (44a) and (44b), it can be seen that the steady-state terms must satisfy

$$\gamma_{mn}(2\mathcal{K}_3 - S) + \mu_{mn}^2 \mathcal{C}_{mn} = 0, \tag{47a}$$

$$S\sum_{n=1}^{\infty} g_{nk}\left[\frac{\gamma_{mn}}{\mu_{mn}^2}(2\mathcal{K}_3 - S) + \mathcal{C}_{mn}\cosh(\mu_{mn}h) - \mathcal{D}_{mn}\sinh(\mu_{mn}h)\right] + \eta\mu_{mk}^2[\mathcal{C}_{mk}\cosh(\mu_{mk}h) - \mathcal{D}_{mn}\sinh(\mu_{mk}h)] + \eta\gamma_{mk}(2\mathcal{K}_3 - S) = 0, \tag{47b}$$

together with (43). From Eq. (47a) we see that

$$\mathcal{C}_{mn} = -\frac{\gamma_{mn}}{\mu_{mn}^2}(2\mathcal{K}_3 - S). \tag{48}$$

If we now let $\eta \to 0$ in Eq. (47b) we have

$$\frac{\gamma_{mn}}{\mu_{mn}^2}(2\mathcal{K}_3 - S) + \mathcal{C}_{mn}\cosh(\mu_{mn}h) - \mathcal{D}_{mn}\sinh(\mu_{mn}h) = 0. \tag{49}$$

From this equation, we determine that

$$\mathcal{D}_{mn} = (2\mathcal{K}_3 - S)\frac{\gamma_{mn}}{\mu_{mn}^2}\left[\frac{1 - \cosh(\mu_{mn}h)}{\sinh(\mu_{mn}h)}\right]. \tag{50}$$

Substitution into (43) gives

$$2h\mathcal{K}_3 + \frac{(2\mathcal{K}_3 - S)}{2}\sum_{m=1}^{\infty}\sum_{n=1}^{\infty}\frac{\gamma_{mn}^2}{\mu_{mn}}\left[\frac{1 - \cosh(\mu_{mn}h)}{\sinh(\mu_{mn}h)}\right] = 0. \tag{51}$$

Solving, we obtain

$$\mathcal{K}_3 = \frac{S\sigma}{2(2h + \sigma)}, \quad \sigma \equiv \sum_{m=1}^{\infty}\sum_{n=1}^{\infty}\frac{\gamma_{mn}^2}{\mu_{mn}}\left[\frac{1 - \cosh(\mu_{mn}h)}{\sinh(\mu_{mn}h)}\right]. \tag{52}$$

Then, the coefficients are

$$\mathcal{C}_{mn} = \frac{S\gamma_{mn}}{\mu_{mn}^2}\left(\frac{2h}{2h + \sigma}\right), \qquad \mathcal{D}_{mn} = -\left[\frac{1 - \cosh(\mu_{mn}h)}{\sinh(\mu_{mn}h)}\right]\mathcal{C}_{mn}. \tag{53}$$

Note too that

$$\mathcal{K}_2 = -h\mathcal{K}_3. \tag{54}$$

F. Unsteady portion of the solution

Substituting (46a)–(46c) into Eqs. (43), (44a), and (44b), and looking for solutions of the form $(C_{mn}, D_{mn}, K_i) = (c_{mn}, d_{mn}, k_i)\exp(\lambda\tau)$, gives

$$2hk_3 + \frac{1}{4}\sum_{m=1}^{\infty}\sum_{n=1}^{\infty}\mu_{mn}\gamma_{mn}\left\{d_{mn}[1-\cosh(\mu_{mn}h)] + c_{mn}\sinh(\mu_{mn}h)\right\} = 0, \tag{55a}$$

$$\lambda\mu_{mk}d_{mk} - \frac{\lambda}{4}\gamma_{mk}\sum_{r=1}^{\infty}\sum_{s=1}^{\infty}\mu_{rs}\gamma_{rs}d_{rs} = -\eta\gamma_{mk}2k_3 - \eta\mu_{mk}^2 c_{mk}, \tag{55b}$$

$$\begin{aligned}\lambda\mu_{mk}d_{mk}\cosh(\mu_{mk}h) - \lambda\mu_{mk}c_{mk}\sinh(\mu_{mk}h)\\ - \frac{\lambda}{4}\gamma_{mk}\sum_{r=1}^{\infty}\sum_{s=1}^{\infty}\gamma_{rs}\mu_{rs}\left[d_{rs}\cosh(\mu_{rs}h) - c_{rs}\sinh(\mu_{rs}h)\right]\\ = S\sum_{n=1}^{\infty}g_{kn}\left[2k_3\frac{\gamma_{mn}}{\mu_{mn}^2} + c_{mn}\cosh(\mu_{mn}h) - d_{mn}\sinh(\mu_{mn}h)\right]\\ + \eta\mu_{mk}^2 c_{mk}\cosh(\mu_{mk}h) - \eta\mu_{mk}^2 d_{mk}\sinh(\mu_{mk}h) + \eta\gamma_{mk}2k_3.\end{aligned} \tag{55c}$$

If we now recall that η is small, then one can take the limit $\eta \to 0$, to obtain small-η approximations to the solution. It is evident from (55) that quite different results for the limit will occur, depending on the assumed order of λ. So, evidently, two families of eigenvalues/eigenvectors arise. There is a subsequent difficulty with the $\eta \to 0$ limit, to which we shall return later in the discussion.

1. Small-λ eigensolutions: $\lambda = \mathcal{O}(\eta)$

We begin by assuming that $\lambda = \mathcal{O}(\eta)$, by writing $\lambda = \eta\Lambda$, and then passing to the limit. Denoting the leading-order solutions in this case by $\tilde{c}_{mn}$, $\tilde{d}_{mn}$, and $\tilde{k}_3$, we have, from (55a)–(55c),

$$2\tilde{k}_3 h + \frac{1}{4}\sum_{m=1}^{\infty}\sum_{n=1}^{\infty}\mu_{mn}\gamma_{mn}\left\{\tilde{d}_{mn}[1-\cosh(\mu_{mn}h)] + \tilde{c}_{mn}\sinh(\mu_{mn}h)\right\} = 0, \tag{56a}$$

$$\Lambda\mu_{mn}\tilde{d}_{mn} - \frac{\Lambda}{4}\gamma_{mn}\sum_{r=1}^{\infty}\sum_{s=1}^{\infty}\mu_{rs}\gamma_{rs}\tilde{d}_{rs} = -2\gamma_{mn}\tilde{k}_3 - \mu_{mn}^2\tilde{c}_{mn}, \tag{56b}$$

$$\frac{\gamma_{mn}}{\mu_{mn}^2}2\tilde{k}_3 + \cosh(\mu_{mn}h)\tilde{c}_{mn} - \sinh(\mu_{mn}h)\tilde{d}_{mn} = 0. \tag{56c}$$

Solving Eq. (56c) for $\tilde{c}_{mn}$ gives

$$\tilde{c}_{mn} = \tanh(\mu_{mn}h)\tilde{d}_{mn} - \frac{\gamma_{mn}}{\mu_{mn}^2\cosh(\mu_{mn}h)}2\tilde{k}_3. \tag{57}$$

Substitution of this expression into (56a) and collecting terms leads to

$$2\tilde{k}_3 = -\frac{1}{4Z}\sum_{m=1}^{\infty}\sum_{n=1}^{\infty}\mu_{mn}\gamma_{mn}\Gamma_{mn}\tilde{d}_{mn}, \tag{58}$$

where

$$Z \equiv h - \frac{1}{4}\sum_{m=1}^{\infty}\sum_{n=1}^{\infty}\frac{\gamma_{mn}^2}{\mu_{mn}}\tanh(\mu_{mn}h),$$

$$\Gamma_{mn} \equiv 1 - \operatorname{sech}(\mu_{mn}h).$$

Then, substitution for $\tilde{k}_3$ from (58) and $\tilde{c}_{mn}$ from (57) into (56b) gives

$$S_{mn} = \frac{\Lambda}{4}\frac{\gamma_{mn}}{\Lambda + \mu_{mn}\tanh(\mu_{mn}h)}\sum_{r=1}^{\infty}\sum_{s=1}^{\infty}\gamma_{rs}S_{rs} + \frac{1}{4Z}\frac{\gamma_{mn}\Gamma_{mn}}{\Lambda + \mu_{mn}\tanh(\mu_{mn}h)}\sum_{r=1}^{\infty}\sum_{s=1}^{\infty}\gamma_{rs}\Gamma_{rs}S_{rs}, \tag{59}$$

where

$$S_{mn} \equiv \mu_{mn}\tilde{d}_{mn}. \tag{60}$$

Multiplying this equation through by γ_{mn} and summing over m, n, then a second time multiplying through by $\gamma_{mn}\Gamma_{mn}$, and summing, gives a pair of homogeneous equations for the two doubly infinite series on the right side of (59). Putting the determinant of that system to zero gives the eigenvalue problem for Λ, namely,

$$1 - \frac{\Lambda}{4}\sum_{m=1}^{\infty}\sum_{n=1}^{\infty}\frac{\gamma_{mn}^2}{\Lambda + \mu_{mn}\tanh(\mu_{mn}h)} - \frac{1}{4Z}\sum_{m=1}^{\infty}\sum_{n=1}^{\infty}\frac{\gamma_{mn}^2\Gamma_{mn}^2}{\Lambda + \mu_{mn}\tanh(\mu_{mn}h)} + \frac{\Lambda}{16Z}\left[\left(\sum_{m=1}^{\infty}\sum_{n=1}^{\infty}\frac{\gamma_{mn}^2}{\Lambda + \mu_{mn}\tanh(\mu_{mn}h)}\right)\left(\sum_{m=1}^{\infty}\sum_{n=1}^{\infty}\frac{\gamma_{mn}^2\Gamma_{mn}^2}{\Lambda + \mu_{mn}\tanh(\mu_{mn}h)}\right) - \left(\sum_{m=1}^{\infty}\sum_{n=1}^{\infty}\frac{\gamma_{mn}^2\Gamma_{mn}}{\Lambda + \mu_{mn}\tanh(\mu_{mn}h)}\right)^2\right] = 0. \tag{61}$$

Once an eigenvalue has been found, the eigenvector corresponding to Λ_β is given by

$$S_{mn\beta} = \mu_{mn}\tilde{d}_{mn} = c_\beta\mu_{mn}V_{mn\beta}, \tag{62}$$

where

$$V_{mn\beta} = \frac{1}{u_{mn\beta}}\left\{\sum_{r=1}^{\infty}\sum_{s=1}^{\infty}\frac{\gamma_{rs}^2\Gamma_{rs}}{u_{rs\beta}}\left(\Gamma_{mn} + \frac{\Lambda_\beta}{4}\left[\sum_{r=1}^{\infty}\sum_{s=1}^{\infty}\frac{\gamma_{rs}^2\Gamma_{rs}}{u_{rs\beta}} - \Gamma_{mn}\sum_{r=1}^{\infty}\sum_{s=1}^{\infty}\frac{\gamma_{rs}^2}{u_{rs\beta}}\right]\right)\right\}, \tag{63a}$$

$$u_{mn\beta} = \frac{\mu_{mn}}{\gamma_{mn}}\left[\Lambda_\beta + \mu_{mn}\tanh(\mu_{mn}h)\right]. \tag{63b}$$

Then, the general solution for this segment of the initial-value problem is

$$\tilde{d}_{mn} = \sum_{\beta=1}^{\infty}c_\beta V_{mn\beta}e^{\eta\Lambda_\beta\tau}. \tag{64}$$

Computationally, it turns out that there are no real and positive solutions of (61) – the only solutions appear to be real and negative. Truncating the series at N, the upper limit on the sum in (62) is $\mathcal{M}$ since there are $\mathcal{M}(N)$ eigenvalues distributed over negative real values, beginning with Λ_o, that is, for all solutions, $\Lambda_i \le \Lambda_o(S)$. We have determined from analysis and confirmed with computation that $\mathcal{M} = (N+1)(N+3)/8$. From computations using 100 terms in the series (showing no significant difference from a 50-term result), results are shown in Table II.

So, these no-wave modes decay quite rapidly on the α^{-1} time scale.

TABLE II. Values for Λ_o for representative values of S (using 100 terms in the series).

S	Λ_o
0.5	− 2.41
1.0	− 3.51
2.0	− 5.07
5.0	− 8.20

2. Eigenmodes for $\lambda = \mathcal{O}(1)$: Rossby waves

If we now take $\lambda = \mathcal{O}(1)$, then Eq. (55b) shows that $d_{mn} = \mathcal{O}(\eta)$. We then expand c_{mn}, d_{mn}, k_3, and λ in powers of η, as

$$c_{mn} = c_{mn}^{(0)} + \eta c_{mn}^{(1)} + \ldots, \tag{65a}$$

$$d_{mn} = \eta d_{mn}^{(1)} + \ldots, \tag{65b}$$

$$k_3 = k_3^{(0)} + \eta k_3^{(1)} + \ldots, \tag{65c}$$

$$\lambda = \lambda_0 + \eta\lambda_1 + \ldots. \tag{65d}$$

The leading-order components of Eqs. (55a) and (55c) are then

$$2hk_3^{(0)} + \frac{1}{4}\sum_{m=1}^{\infty}\sum_{n=1}^{\infty}\mu_{mn}\gamma_{mn}c_{mn}^{(0)}\sinh(\mu_{mn}h) = 0. \tag{66a}$$

$$-\lambda_0\mu_{mk}c_{mk}^{(0)}\sinh(\mu_{mk}h) + \frac{\lambda_0}{4}\gamma_{mk}\sum_{r=1}^{\infty}\sum_{s=1}^{\infty}\gamma_{rs}\mu_{rs}c_{rs}^{(0)}\sinh(\mu_{rs}h) = S\sum_{n=1}^{\infty}g_{kn}\left[2k_3^{(0)}\frac{\gamma_{mn}}{\mu_{mn}^2} + c_{mn}^{(0)}\cosh(\mu_{mn}h)\right]. \tag{66b}$$

Combining these equations, with the definition

$$\Phi_n^{(m)} \equiv \mu_{mn}\sinh(\mu_{mn}h)c_{mn}^{(0)},$$

leads eventually to

$$\lambda_0\Phi_k^{(m)} + S\sum_{n=1}^{\infty}g_{kn}\frac{\coth(\mu_{mn}h)}{\mu_{mn}}\Phi_n^{(m)} = E_k^{(m)}U, \tag{67}$$

where for convenience, we have defined

$$U \equiv \sum_{r=1}^{\infty}\sum_{s=1}^{\infty}\gamma_{rs}\Phi_s^{(r)}, \qquad H_{mk} \equiv S\sum_{n=1}^{\infty}g_{kn}\frac{\gamma_{mn}}{\mu_{mn}^2} \tag{68a}$$

and

$$E_k^{(m)} \equiv \frac{\lambda}{4}\gamma_{mk} + \frac{1}{4h}H_{mk}. \tag{68b}$$

In order to solve the problem computationally, we truncate the series at N terms. Hence, in matrix notation this is the N-dimensional system

$$\left(\lambda_0\mathrm{I} + Sg\mathrm{D}_m\right)\boldsymbol{\Phi}^{(m)} = \mathbf{E}^{(m)}U, \tag{69}$$

with

$$\mathrm{D}_m = \left[d_{ij}^{(m)}\right], \quad d_{ij}^{(m)} = \frac{\coth(\mu_{mi}h)}{\mu_{mi}}\,\delta_{ij}. \tag{70}$$

Let an eigenvector of (69) be written as

$$\mathbf{\Phi}^{(m)} = \mathbf{T}^{(m)}U, \tag{71}$$

where

$$\mathbf{T}^{(m)} = \left[\lambda_0 + SgD_m\right]^{-1}\mathbf{E}^{(m)}. \tag{72}$$

So, the nth element of (71) is

$$\Phi_n^{(m)} = T_n^{(m)}U. \tag{73}$$

Multiplying this equation by γ_{mn} and summing over m and n, the quantity on the left-hand-side is U, and so we have

$$U\left[1 - \sum_{r=1}^{\infty}\sum_{s=1}^{\infty}\gamma_{rs}T_s^{(r)}\right] = 0. \tag{74}$$

Setting the square bracket to zero gives the equation for the eigenvalues,

$$\sum_{r=1}^{\infty}\sum_{s=1}^{\infty}\gamma_{rs}T_s^{(r)} = 1. \tag{75}$$

We consider here only even values of N (odd values introduce spurious zero eigenvalues). Truncation of the series at N terms leads to $N^2/2 \equiv \mathcal{N}$ eigenvalues. Details of the counting, and the computation of the frequencies are given in Appendix A, where we determine that all of the eigenvalues form conjugate, imaginary pairs, so there are $\mathcal{N}/2$ distinct frequencies. In Table III we tabulate the frequency ranges for λ_0, for four values of S with $N = 100$. It is interesting to note that the range of frequencies for the (75) problem is closely related to the range of frequencies for the homogeneous problem $(\lambda\mathrm{I} + SgD_m)\mathbf{\Phi}^{(m)} = \mathbf{0}$. In fact, as $N \to \infty$, the frequencies at the upper and lower ends of the spectrum for $|\lambda_0|$ are identical to the smallest and largest eigenvalues for the homogeneous problem. The way the frequencies are distributed inside that interval is quite complicated, and not identical with the distribution of frequencies for the homogeneous problem. Further, all values of $|\lambda_0|$ lie between 0 and $\sqrt{S}$.

The formal writing down of infinite series is meaningless, of course, unless those series can be seen to be convergent. Here, the vector $\mathbf{E}^{(m)}$ can be seen to behave like $\mathbf{q}_m$ for $m \to \infty$, and from (72), $\mathbf{T}^{(m)}$ has the same behaviour for $m \to \infty$. Therefore, the sum in (75), which can be written as

$$\sum_{r=1}^{\infty} q_r \mathbf{q}^{\mathrm{T}}\mathbf{T}^{(r)} \sim \sum_{r=1}^{\infty}\frac{q_r}{r}|\mathbf{q}|^2,$$

TABLE III. Frequency range for λ_0 for several values of S (for $N = 100$).

S	Range for $\lvert\lambda_0\rvert$
0.5	0.00701–0.707
0.5[a]	0.00694–0.707
1.0	0.0101–0.995
1.0[a]	0.00981–1.00
2.0	0.0140–1.41
2.0[a]	0.0139–1.41
5.0	0.0222–2.24
5.0[a]	0.0219–2.24

[a]Minimum and maximum frequencies associated with the matrix SgD_m, for all $1 \le m \le N$.

converges like that of the series $\sum_r 1/r^2$. This argument may be made rigorous. This weak $1/r$ behaviour of $\mathbf{T}^{(r)}$ for large r will be the source of some difficulty later in the theoretical development.

3. Eigenmodes for $\lambda = \mathcal{O}(1)$: Frictional decay of Rossby waves

We now return to the general eigenvalue problem (55a)–(55c), insert the asymptotic expansion defined in (65), and examine the equation for the order η terms, in order to determine λ_1. Recall that $d_{mn}^{(0)} = 0$ in this case. If we define

$$\mu_{mn}\sinh(\mu_{mn}h)c_{mn}^{(1)} \equiv \hat{\Phi}_n^{(m)}, \quad \mu_{mn}\cosh(\mu_{mn}h)d_{mn}^{(1)} \equiv \Psi_n^{(m)}, \tag{76}$$

then from (55a)–(55c), and anticipating series truncation, and hence using matrix notation, we obtain the respective results:

$$2hk_3^{(1)} + \frac{1}{4}\sum_{m=1}^{\infty}\sum_{n=1}^{\infty} q_m \mathbf{q}^{\mathrm{T}}\left[\hat{\mathbf{\Phi}}^{(m)} + \left(\mathcal{B}_m - \mathrm{I}\right)\mathbf{\Psi}^{(m)}\right] = 0, \tag{77a}$$

$$\lambda_0 \mathcal{B}_m \mathbf{\Psi}^{(m)} - \frac{\lambda_0}{4} q_m \mathbf{q}\sum_{r=1}^{\infty} q_r \mathbf{q}^{\mathrm{T}}\mathcal{B}_r \mathbf{\Psi}^{(r)} = -2k_3^{(0)} q_m \mathbf{q} - \mathcal{F}_m \mathbf{\Phi}^{(m)}. \tag{77b}$$

$$\begin{aligned}\lambda_0\left(\mathbf{\Psi}^{(m)} - \hat{\mathbf{\Phi}}^{(m)}\right) - \frac{\lambda_0}{4} q_m \mathbf{q}\sum_{r=1}^{\infty} q_r \mathbf{q}^{\mathrm{T}}\left(\mathbf{\Psi}^{(r)} - \hat{\mathbf{\Phi}}^{(r)}\right)\\ - \lambda_1 \mathbf{\Phi}^{(m)} + \frac{\lambda_1}{4} q_m \mathbf{q}\sum_{r=1}^{\infty} q_r \mathbf{q}^{\mathrm{T}}\mathbf{\Phi}^{(r)} - \mathcal{A}_m \mathbf{\Phi}^{(m)}\\ = 2k_3^{(1)}\mathbf{H}_m + Sg\mathrm{D}_m\hat{\mathbf{\Phi}}^{(m)} - Sg\hat{\mathrm{D}}_m\mathbf{\Psi}^{(m)} + 2q_m\mathbf{q}k_3^{(0)}.\end{aligned} \tag{77c}$$

Four diagonal matrices have arisen here. They are defined by

$$\mathcal{A}_m = \left[\delta_{ij}\mu_{mi}\coth(\mu_{mi}h)\right], \qquad \mathcal{B}_m = \left[\delta_{ij}\mathrm{sech}(\mu_{mi}h)\right], \tag{78a}$$

$$\mathcal{F}_m = \left[\delta_{ij}\mu_{mi}\mathrm{csch}(\mu_{mi}h)\right], \qquad \hat{\mathrm{D}}_m = \left[\delta_{ij}\tanh(\mu_{mi}h)/\mu_{mi}\right]. \tag{78b}$$

The solution to Eq. (77b) may be most conveniently written in terms of an arbitrary constant $\hat{c}$, and is

$$\mathbf{\Psi}^{(m)} = q_m \mathcal{B}_m^{-1}\mathbf{q}\left[\hat{c} - \frac{2k_3^{(0)}}{\lambda_0}\right] - \frac{1}{\lambda_0}\mathcal{B}_m^{-1}\mathcal{F}_m\mathbf{\Phi}^{(m)}. \tag{79}$$

It turns out that the first term leads to divergent series in what follows, so we choose $\hat{c}$ to make the square bracket vanish. Inserting $k_3^{(0)}$ and $k_3^{(1)}$ into this equation and rearranging gives

$$\begin{aligned}\left(\lambda_0 + Sg\mathrm{D}_m\right)\hat{\mathbf{\Phi}}^{(m)} - \frac{\mathbf{H}_m}{4h}\sum_{r=1}^{\infty} q_r\mathbf{q}^{\mathrm{T}}\hat{\mathbf{\Phi}}^{(r)} - \frac{\lambda_0}{4}q_m\mathbf{q}\sum_{r=1}^{\infty} q_r\mathbf{q}^{\mathrm{T}}\hat{\mathbf{\Phi}}^{(r)}\\ = \left(\lambda_0 + Sg\hat{\mathrm{D}}_m\right)\hat{\mathbf{\Psi}}^{(m)} - \frac{\lambda_0}{4}q_m\mathbf{q}\sum_{r=1}^{\infty} q_r\mathbf{q}^{\mathrm{T}}\mathbf{\Psi}^{(r)} - \left(\lambda_1 + \mathcal{A}_m\right)\mathbf{\Phi}^{(m)}\\ + \frac{\lambda_1}{4}q_m\mathbf{q}\sum_{r=1}^{\infty} q_r\mathbf{q}^{\mathrm{T}}\mathbf{\Phi}^{(r)} + \frac{q_m\mathbf{q}}{4h}\sum_{r=1}^{\infty} q_r\mathbf{q}^{\mathrm{T}}\mathbf{\Phi}^{(r)} + \frac{\mathbf{H}_m}{4h}\sum_{r=1}^{\infty} q_r\mathbf{q}^{\mathrm{T}}\left(\mathcal{B}_r - \mathrm{I}\right)\mathbf{\Psi}^{(r)}.\end{aligned} \tag{80}$$

For convenience in writing what follows, we put

$$U_0 \equiv \sum_{r=1}^{\infty} q_r\mathbf{q}^{\mathrm{T}}\mathbf{\Phi}^{(r)}, \quad U_1 \equiv \sum_{r=1}^{\infty} q_r\mathbf{q}^{\mathrm{T}}\hat{\mathbf{\Phi}}^{(r)}.$$

Further, let

$$K_{mj} = \left(\lambda_{0j}\mathrm{I} + Sg\mathrm{D}_m\right)^{-1}, \tag{81}$$

where λ_{0j} is the jth eigenvalue. We may then solve for $\hat{\mathbf{\Phi}}^{(m)}$, which becomes the correction to the leading-order eigenfunction. Therefore,

$$\begin{aligned}\hat{\mathbf{\Phi}}^{(m)} - K_{mj}\frac{\mathbf{H}_m}{4h}U_1 - \frac{\lambda_{0j}}{4}q_m K_{mj}\mathbf{q}U_1 \\ = K_{mj}\left(\lambda_{0j} + Sg\hat{\mathrm{D}}_m\right)\mathbf{\Psi}^{(m)} - \frac{\lambda_{0j}}{4}q_m K_{mj}\mathbf{q}\sum_{r=1}^{\infty} q_r \mathbf{q}^{\mathrm{T}}\mathbf{\Psi}^{(r)} - K_{mj}\left(\lambda_1 + \mathcal{A}_m\right)\mathbf{\Phi}^{(m)} \\ + \frac{\lambda_1}{4}q_m K_{mj}\mathbf{q}U_{0j} + \frac{q_m K_{mj}\mathbf{q}}{4h}U_{0j} + \frac{K_{mj}\mathbf{H}_m}{4h}\sum_{r=1}^{\infty} q_r \mathbf{q}^{\mathrm{T}}\left(\mathcal{B}_r - \mathrm{I}\right)\mathbf{\Psi}^{(r)}.\end{aligned} \tag{82}$$

For the moment, let the right side of this equation be denoted by $\boldsymbol{\mathcal{S}}^{(m)} + \lambda_1\boldsymbol{\mathcal{T}}^{(m)}$. We multiply through by $q_m\mathbf{q}^{\mathrm{T}}$, and sum over m. What results is

$$\left(1 - \sum_{m=1}^{\infty} q_m \mathbf{q}^{\mathrm{T}} K_{mj}\frac{\mathbf{H}_m}{4h} - \frac{\lambda_{0j}}{4}\sum_{m=1}^{\infty} q_m^2 \mathbf{q}^{\mathrm{T}} K_{mj}\mathbf{q}\right)U_1 = \sum_{m=1}^{\infty} q_m \mathbf{q}^{\mathrm{T}}\left[\boldsymbol{\mathcal{S}}^{(m)} + \lambda_1\boldsymbol{\mathcal{T}}^{(m)}\right]. \tag{83}$$

The bracketed term on the left-hand side is identically zero, hence the right side must be zero, which gives the $\mathcal{O}(\eta)$ correction to the eigenvalue, namely,

$$\lambda_{1j} = -\sum_{m=1}^{\infty} q_m \mathbf{q}^{\mathrm{T}}\boldsymbol{\mathcal{S}}^{(m)} \Big/ \sum_{m=1}^{\infty} q_m \mathbf{q}^{\mathrm{T}}\boldsymbol{\mathcal{T}}^{(m)}. \tag{84}$$

Appendix B contains the formulae for the sums in the quotient in terms of various sums over $\mathbf{\Phi}^{(m)}$ and details about the computation of $\{\lambda_{1j}\}$.

A serious difficulty arises when computing the several terms found in Appendix B that constitute the terms in (84): Some of the constituent series are divergent. That problem arises from the apparently näive form of the asymptotic expansion given by (65). The trouble is evident in Eq. (55c). We have retained the second term on the left side of the equation, $\lambda\mu_{mk}c_{mk}\sinh(\mu_{mk}h)$, as a leading-order term in the asymptotic series, but dropped term $\eta\mu_{mk}^2 c_{mk}\cosh(\mu_{mk}h)$ on the right side. Clearly, both terms are of identical order if $\eta\mu_{mk} = \mathcal{O}(1)$, which will be so for sufficiently large m or k. In fact, the second term is dominant as $n, k \to \infty$. So, it is this second term that ultimately guarantees convergent series in (84). Said another way, the asymptotic expansion (65) is not uniformly valid in (m, n). Separating out this non-uniformity by standard matched asymptotic expansion methods has so far eluded us. As an alternative, in the computation of the constituent series sums in (84), we use $\mathbf{\Phi}^{(m)}$ determined not from solution to (69), but from a modified form that includes this requisite term,

$$\left(\lambda_0\mathrm{I} + Sg\mathrm{D}_m + \eta\mathcal{A}_m\right)\mathbf{\Phi}^{(m)} = \mathbf{E}^{(m)}U, \tag{85}$$

so now $\mathbf{\Phi}^{(m)} \sim 1/(\eta m^2)$ for $m \to \infty$. That change leads to $o(1)$ effects on the Rossby wave frequencies, but makes it possible to compute λ_1.

Since η is included in the above equation, computed values for $\mathbf{\Phi}^{(m)}$ and the series in (84) depend on η as well. We have carefully computed values for the damping coefficient, λ_{1k} for representative values of λ_{0k}, then extrapolated for $N \to \infty$. Each N-extrapolated λ_{1k} is then a function of η. We have examined the η-dependence of these N-extrapolated numbers, and have noted that the computations give a particular logarithmic dependence on η, which we show in Appendix B is precisely what one would predict. We have found that

$$\lambda_{1k} = a_k(S) + b_k(S)\log\eta,$$

TABLE IV. For $\lambda_{1k} = a_k + b_k \log \eta$, the real values of a_k and b_k for some typical values at each of five values of S. All values have been extrapolated to $N \to \infty$. Note that, since $\eta \ll 1$, it follows that $\log \eta$ is large and negative. In these calculations, $h = 1$. The final column shows the total value of λ_{1k} for $\eta = 0.02$.

S	$\lvert\lambda_{0k}\rvert$	$\Re\text{eal}\{a_k\}$	$\Re\text{eal}\{b_k\}$	$\Re\text{eal}\{\lambda_{1k}\}$
0.0	$\leq$0.225	− 2.00	0.00	− 2.00
0.5	0.464	8.90	3.35	− 4.20
	0.710	1.95	2.70	− 8.61
1.0	0.497	24.0	7.48	− 5.26
	1.00	− 5.89	1.13	− 10.3
2.0	1.03	6.90	4.20	− 9.53
	1.41	− 12.8	0.773	− 15.9
5.0	0.948	77.7	22.0	− 8.36
	2.24	− 26.2	0.571	− 44.2

for the η-dependence of each λ_{1k} for η small. Moreover, λ_{1k} turns out to be complex, so in addition to damping, there is a correction to the frequency. Both real and imaginary parts of λ_{1k} appear to have the same dependence on η. Table IV shows values of the real parts of λ_{1k} for selected values of λ_{0k}, for five values of the Burger number, S. Note that the damping coefficients are quite large in general, for order-one values of S. (We have not shown the imaginary parts in Table IV since the small modification to the Rossby-wave frequency is of minor importance only.) We have also not tabulated results for very small values of $|\lambda_{0k}|$, because for $|\lambda_{0k}|$ of order α, these damped Rossby waves merge into the fully damped modes discussed in Sec. III F 1 in some very complicated fashion.

What all of this means is that the actual asymptotic series for a wave-like eigenvalue takes the form

$$\lambda_j = \lambda_{0j} + b_j \eta \log \eta + a_j \eta + \ldots. \tag{86}$$

It is clear from our computations that all values of b_j have positive real part, so from the point of view of the asymptotics, all modes are damped. Even for the cases in the table for which $\Re eal\{a_j\} > 0$, that term is always smaller than the $\eta \log \eta$ term for η sufficiently small. So, for the series for λ to indeed be an asymptotic series, it is not sufficient that $\eta \ll 1$, but we also apparently require that

$$\frac{1}{|\log \eta|} \ll 1.$$

In our experiments, $\eta \sim 0.2$, and $1/|\log(0.2)| \sim 0.6$, unfortunately not small enough for this theory to be valid. The last column of the table shows the real part of λ_1 for a $\eta = 0.02$, for which $1/|\log \eta| = 0.255$—still not very small. By entering the value for $S \equiv 0$—to be taken up briefly in Sec. IV, it certainly appears that b_k goes to zero with S, and a_k to -2. Hence, the trend we see in this theory seems to be borne out by the experiments, where we have found evidence for Rossby waves only at small S.

Therefore, all unsteady components – wave-like and otherwise – vanish for $\alpha \eta \log \eta\, t \to \infty$, leaving only the steady-state solution of Sec. III E. Using the results in that section for $\mathcal{C}_{mn}$, $\mathcal{D}_{mn}$, and $\mathcal{K}_3$, we find that the leading-order pressure is given by

$$\lim_{\eta\tau\to\infty} p_0 = \frac{2h}{2h+\sigma} \sum_{m=1}^{\infty}\sum_{n=1}^{\infty} \frac{S\gamma_{mn}}{\mu_{mn}^2} \left\{ \frac{\cosh[\mu_{mn}(z-h/2)]}{\cosh(\mu_{mn}h/2)} - 1 \right\} \phi_m(x)\phi_n(y) - \frac{S\sigma(h-z)z}{2(2h+\sigma)}, \tag{87}$$

which is identical to the limiting case found for the uniform-depth square cylinder.[14] Recall that σ is defined in (52).

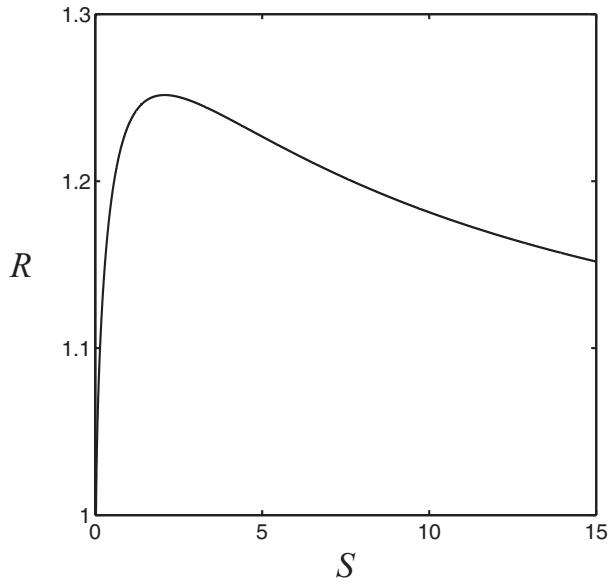

FIG. 7. Ratio (R) of long-time velocity at outer wall to initial value, given in (90), as a function of S. Note that overspin occurs for all values of S.

Interestingly, the limiting value of y-direction velocity component, $v_0 = p_{0x}/2$, evaluated at the $x = 1$ wall, at the mid-plane $z = h/2$, and along the symmetry axis $y = 1/2$, is given by

$$\lim_{\eta\tau\to\infty} v_0(1, 1/2, h/2, \tau) = \frac{\pi h}{2h+\sigma} \sum_{m=1}^{\infty}\sum_{n=1}^{\infty} \frac{S\gamma_{mn}}{\mu_{mn}^2} [\mathrm{sech}(\mu_{mn}h/2) - 1]\, m(-1)^m \sin(n\pi/2). \quad (88)$$

In the uniform-depth case, we found that the mid-plane speed might be larger at large-$\eta\tau$ than it is at the beginning of this process, after the early time dynamics has concluded. From Eq. (19), the early time result is

$$v_0(1, 1/2, h/2)\big|_{\tau=0} = -\frac{\pi}{2} \sum_{m=1}^{\infty}\sum_{n=1}^{\infty} \frac{S\gamma_{mn}}{\mu_{mn}^2} m(-1)^m \sin(n\pi/2). \quad (89)$$

The ratio of these two is

$$R \equiv \frac{v_0(1, 1/2, h/2)|_{\tau=\infty}}{v_0(1, 1/2, h/2)|_{\tau=0}}, \quad (90)$$

and is plotted in Figure 7 for a range of values of S.

There are four observations that may now be made: (1) For large $\eta\tau$, the fluid near upper and lower boundaries is spun up, but not in the central core—just as for the case of the uniform-depth square cylinder.[14] In fact, as in that previous case, this partially spun-up state is fully symmetric about the mid-plane. (2) The long-time state is identical to that found for the uniform-depth cylinder, however, in the sliced cylinder that state arises by a combination of Rossby-wave propagation and frictional decay. Moreover, for the sliced cylinder the frictional decay is somewhat more rapid, occurring on a time scale of order $E^{-1/2}/\log(\alpha/E^{1/2})$, in contrast to the uniform-depth case, for which the damping is ordered with $E^{-1/2}$. Therefore, the presence of even a small slope leads to increased decay rates toward the partially spun-up state. (3) The corner Ekman eruptions come directly into the processes in two ways. First, as with the uniform-depth case,[14] the partially spun-up state depends on the parameter σ, with a curious overshoot in the mid-tank rotation rate—the "over-spin" as indicated in Figure 7. Second, it is precisely these eruptions that lead to the $\eta\log\eta$ term in the λ series. (4) Figure 7 shows that "overspin" occurs in this geometry for all values of $S > 0$; since $R = 1$ when $S = 0$, there is no overspin in the homogeneous case. The maximum overspin occurs at $S = 2.08$, where R is slightly larger than 1.25.

IV. HOMOGENEOUS SPIN-UP

Because the spin-up decay rates are so large in the case of the stratified Rossby waves, a comparison with homogeneous spin-up for this geometry might be instructive, since we know from Pedlosky and Greenspan[10] that the Rossby-wave decay rates are not large, making it possible for those to be observed.

Scaling the time by α as in Sec. III D, and inserting a regular perturbation series in powers of S into Eq. (11) leads to the following equations for the first two terms in the series:

$$p_{0zz} = 0, \qquad p_{1zz} = 1 - \frac{1}{4}\nabla_1^2 p_0. \tag{91}$$

The boundary conditions at top and bottom for the first term, from (24) and (25), are $p_{0z\tau} = 0$, so the solution is

$$p_0 = G(x, y, \tau). \tag{92}$$

Integrating the p_1 equation,

$$p_1 = \left[1 - \frac{1}{4}\nabla_1^2 G\right]\frac{(z-h)^2}{2} + A(x, y, \tau)(z-h). \tag{93}$$

Then, from the next order upper boundary condition (25),

$$p_{1z\tau} = \frac{\eta}{4}\nabla_1^2 G, \tag{94}$$

we have

$$A_\tau = \frac{\eta}{4}\nabla_1^2 G_\tau. \tag{95}$$

The boundary condition on $z = 0$ is, from (24),

$$p_{1z\tau} = -\frac{\eta}{4}\nabla_1^2 G + \frac{1}{2}G_y, \tag{96}$$

so

$$A_\tau + \frac{h}{4}\nabla_1^2 G_\tau = -\frac{\eta}{4}\nabla_1^2 G + \frac{1}{2}G_y. \tag{97}$$

Eliminating the A_τ between the two equations leads to

$$\frac{h}{2}\nabla_1^2 G_\tau = -\eta\nabla_1^2 G + G_y. \tag{98}$$

Notice that this equation has been derived by ignoring the eruptions $\mathcal{E}$ at $z = 0, h$ that were introduced in (37) and (40) to account for singular, corner eruptions. That is consistent, since this solution is not valid all the way to the vertical walls – there are, in general, boundary layers of width $S^{1/2}$ – discussed below.

Since this has the characteristic feature of a two-timing problem, we suppose $G = G(x, y, \tau, \tilde{\tau})$, where $\tilde{\tau} = \eta\tau$. Then, expanding G in an η series as above,

$$\frac{h}{2}\nabla_1^2 G_{0\tau} = G_{0y}. \tag{99}$$

To next order,

$$\frac{h}{2}\nabla_1^2 G_{1\tau} + \frac{h}{2}\nabla_1^2 G_{0\tilde{\tau}} = -\nabla_1^2 G_0 + G_{1y}. \tag{100}$$

To avoid secular growth,

$$\frac{h}{2}\nabla_1^2 G_{0\tilde{\tau}} + \nabla_1^2 G_0 = 0. \tag{101}$$

Therefore,

$$G_0 = \mathcal{G}(x, y, \tau)e^{-2\eta\tau/h}. \tag{102}$$

So, all modes decay with exactly the same rate, as with the circular-cylindrical geometry.[10] In the notation of Table IV, the quantity $a_k = -2/h$ and $b_k \equiv 0$, for all k. So, apparently, b_k drops dramatically to zero with S.

It turns out that the appropriate side-wall condition is that $p = 0$ on all vertical boundaries, we write the solution in the form

$$\mathcal{G} = \sum_{m=1}^{\infty} A_m(y, \tau)\phi_m(x), \tag{103}$$

leading to

$$A_{myy\tau} - m^2\pi^2 A_{m\tau} = \frac{2}{h} A_{my}. \tag{104}$$

Looking for oscillatory solutions, we write $A_m = B_m e^{i\omega\tau}$, and hence

$$B_{myy} - m^2\pi^2 B_m = \frac{2}{i\omega h} B_{my}, \tag{105}$$

and then determining the y-dependence from a substitution $\exp(\lambda y)$ gives

$$\lambda^2 - m^2\pi^2 - \frac{2}{i\omega h}\lambda = 0, \tag{106}$$

whose solutions are

$$\lambda = -\frac{i}{\omega h} \pm \sqrt{m^2\pi^2 - \frac{1}{\omega^2 h^2}}. \tag{107}$$

Requiring $B_m = 0$ at $y = 0$, 1 leads to the requirement

$$\omega_{mn} = \frac{1}{h\pi\sqrt{m^2 + n^2}}, \quad m, n = 1, 2, 3, \ldots, \tag{108}$$

and the solution is then

$$\mathcal{G} = \sum_{m=1}^{\infty}\sum_{n=1}^{\infty} P_{mn} e^{i(\omega_{mn}\tau - y/(\omega_{mn}h))}\phi_m(x)\phi_n(y). \tag{109}$$

Note that all of the frequencies in this $S = 0$ case lie below $0.225/h$. The quantities $\{P_{mn}\}$ are determined by the initial conditions. (This problem may be solved by Laplace transform, and it can be shown that no branch cuts nor other poles are present—only those leading to this residue sum.)

By examination of the side-wall layers, of width $S^{1/2}$, it is easily seen that they are passive, and that the wall condition $p = 0$ is to be applied to this interior solution. Considerations of Ekman eruptions and mass continuity come in this case at higher order. Details are not shown for the sake of brevity.

V. THE SIDE-WALL RAYLEIGH LAYER AND VELOCITY PROFILE COMPARISONS

The boundary-layer analysis is virtually identical to that reported in Foster and Munro,[14] and is not repeated here. Suffice it to say that the side-wall layers are very different from those arising in an axisymmetric spin-up,[5] where putting the radial velocity to zero at the sidewall makes the azimuthal component of Coriolis acceleration zero there, and hence the azimuthal velocity does not slip over the sidewall. So, the boundary layer is a "buoyancy layer," taking the vertical velocity to zero at the wall. In this problem, however, putting the normal component of velocity to zero at the sidewall makes the vertical velocity zero there, but the tangential horizontal velocity component slips over the surface, and hence the sidewall boundary layer takes the tangential horizontal velocity component to zero at the sidewall. So, it turns out that even at exceedingly small Rossby numbers, the side-wall layer is a fully nonlinear Prandtl boundary layer for $t = \mathcal{O}(\epsilon^{-1})$, and the periodic separation and re-attachment of the boundary layers on the four vertical sides of the container are responsible for the corner eddies identified in Sec. II. Again, much more detail on this matter may be found in Foster and Munro.[14]

For sufficiently small times, however, the side-wall layer is a growing Rayleigh layer, so, for example, in the layer on $x = 0$, the dominant terms lead to

$$v_t = E v_{xx}. \tag{110}$$

If we consider the solution of this equation on the spin-up time scale, $\bar{t} = E^{1/2}t$, and write $x = E^{1/4}\xi$, then the scaled equation in that time regime is

$$v_{\bar{t}} = v_{\xi\xi}. \tag{111}$$

Since we have noted that the Rossby waves decay very rapidly on this time scale, over a significant period in the experiments, where $\tau = \mathcal{O}(1)$, the outer velocity to which this boundary-layer solution matches, is essentially steady, and so,

$$v = \tilde{v}_0(0, y, z)\,\mathrm{erf}\left(\frac{\xi}{2\sqrt{\bar{t}}}\right), \tag{112}$$

where $\tilde{v}_0(x, y, z)$ denotes this steady outer velocity defined, using $v_0 = p_{0x}/2$ and the large-$\eta\tau$ limit in (87), as

$$\tilde{v}_0(x, y, z) \equiv \lim_{\eta\tau\to\infty} v_0(x, y, z, \tau) = \frac{\pi h}{2h+\sigma}\sum_{m=1}^{\infty}\sum_{n=1}^{\infty}\frac{S\gamma_{mn}}{\mu_{mn}^2}\left\{\frac{\cosh[\mu_{mn}(z-h/2)]}{\cosh(\mu_{mn}h/2)} - 1\right\} m\zeta_m(x)\phi_n(y), \tag{113}$$

where

$$\zeta_m(x) = \cos(m\pi x). \tag{114}$$

We can now compare the theory with the experiments. Before proceeding we reiterate that the theoretical results are derived for the condition that $0 < \epsilon \ll E^{1/2}$. Under this regime the sidewall boundary layers, on the spin-up time scale $E^{-1/2}$, are inwardly growing Rayleigh layers, with the formation of the cyclonic corner eddies occurring on the much longer time scale ϵ^{-1}. However, Table I shows that the experimental parameters contradict this condition, with $\epsilon \sim 10E^{1/2}$, and so in the experiments we see the corner eddies forming on time scale notably shorter than the spin-up time scale. Hence, to facilitate meaningful comparisons, we avoid the corner regions and follow the approach adopted by Foster and Munro[14] by comparing the theoretical and experimental values of the horizontal velocity component v, evaluated along the symmetry axis $y = 1/2$, where we expect the effect of the corner-cell formation on the interior flow in the experimental data to be minimal. In this case, Rayleigh layers are needed at $x = 0$ and $x = 1$, and so the required composite solution for v, along $y = 1/2$, is given by

$$v(x, z, \bar{t}) \approx \frac{\pi h}{2h+\sigma}\sum_{m=1}^{\infty}\sum_{n=1}^{\infty}\frac{S\gamma_{mn}}{\mu_{mn}^2}\left\{\frac{\cosh[\mu_{mn}(z-h/2)]}{\cosh(\mu_{mn}h/2)} - 1\right\} m\zeta_m(x)\sin(n\pi/2) + \tilde{v}_0(0, 1/2, z)\,\mathrm{erf}\left(\frac{x}{2\sqrt{E^{1/2}\bar{t}}}\right) - \tilde{v}_0(1, 1/2, z)\,\mathrm{erf}\left(\frac{1-x}{2\sqrt{E^{1/2}\bar{t}}}\right). \tag{115}$$

Figure 8 shows measurements from experiment C ($S = 4.46$) compared with the composite solution in Eq. (115) (see caption for details). The data shown are for times $\bar{t} = E^{1/2}t \geqslant 1$. Clearly, the agreement between theory and experiment is generally excellent at each time shown. This comparison is representative of the agreement found, on the spin-up time scale, for the other four experiments listed in Table I.

VI. FINAL REMARKS

Here we have reported observations from laboratory experiments on the linear spin-up of a linearly stratified fluid in a sliced, square cylinder. We have also constructed a self-consistent

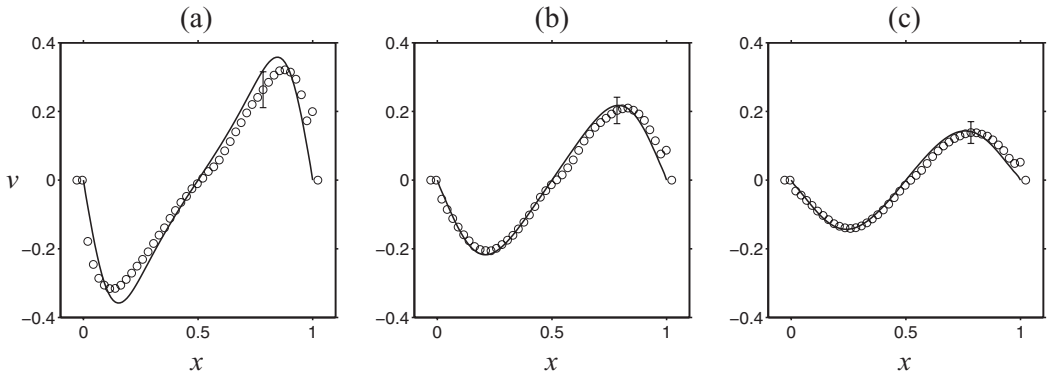

FIG. 8. Experiment C ($\Omega = 0.429\,\text{rad/s}$, $\epsilon = 0.0254$, $S = 4.46$, $z_0/H = 0.329$): Solid lines show the composite solution $v(x, z, \tau)$, along the symmetry axis $y = 1/2$ (defined in Eq. (115)), evaluated at height $z = 0.329h$ and at dimensionless times (a) $\bar{t} = E^{1/2}\Omega t^* = 1.2$, (b) $\bar{t} = 2.9$, and (c) $\bar{t} = 4.4$. The data points (○) show corresponding experimental data. Each velocity profile is an average of data taken over a 2 s period, and the error bar shown is representative of the peak variability observed over this duration.

asymptotic solution for this configuration, under the restrictions $\epsilon \ll E^{1/2} \ll \alpha \ll E^{1/4}$, and have compared and contrasted results from each investigation. The principal results and observations are summarised below.

At early times, the observed flow within the bulk interior (away from base slope) takes the form of a single anticyclone centred about the rotation axis. The streamline pattern and velocity profile exhibit excellent agreement with the theoretical results reported previously by Ref. 14 for the case of a uniform-depth square cylinder. The streamfunction for this flow is derived on the basis that the starting flow is essentially inviscid, two-dimensional and conserves the vorticity of the initial condition. Similar results have been reported previously for other asymmetric geometries.[12,13,20,21] Effects due to the base-slope are evident only in the near-base region, where the centre of the anticyclonic cell is observed to be shifted slightly towards the deeper side of the container.

At the end of the evolution on the spin-up time scale, the limiting form of the outer flow is found to be identical to that found for the spin-up in a uniform-depth square cylinder.[14] However, in this case, stratified Rossby waves, as in the homogeneous counterpart,[10] accomplish the spin-up, together with the Ekman-layer eruptions. The wave spectrum is complicated, the frequencies being solutions of a nonlinear eigenvalue problem. The double Fourier-series used for the solution has buried within it a non-uniformity of the Fourier-series coefficients in the limit $\eta \to 0$. This non-uniformity leads to more rapid damping than that found for the uniform-depth cylinder (where damping occurred on the $E^{-1/2}$ time scale), occurring here on a time scale of order $E^{-1/2}/\log(\alpha/E^{1/2})$. A careful examination of the experimental data seems at first to offer troubling information, where there was little evidence of the Rossby waves. However, for the range of S easily accessible in our laboratory – typically $S \gtrsim \mathcal{O}(1)$ – the damping coefficients were found to be numerically large (Table IV) and to increase with S, suggesting that the Rossby waves damp out very quickly. We found that for $S \sim \mathcal{O}(0.1)$, and only during the early stages, the Rossby modes are detectible.

Periodic side-wall boundary-layer eruption, eddy shedding, formation of cyclonic corner eddies, and then reattachment are ubiquitous features of all of the experiments, regardless of the smallness of the Rossby number; the side-wall boundary layers are inherently nonlinear. Nonetheless, the eddies remain confined to the corner regions. As in the case of the uniform-depth cylinder,[14] the restriction $\epsilon \ll E^{1/2}$, required by the asymptotics, is not satisfied in our experiments, where typically $\epsilon \sim 10E^{1/2}$. In spite of this difficulty, the composite velocity profiles of the long-time outer solution and the side-wall Rayleigh layers are found to agree remarkably well the experimental data, when compared along the symmetry axes $x = 0$ (likewise, similar agreement – not shown here – was found for comparisons of u along the symmetry axis $y = 0$).

ACKNOWLEDGMENTS

M.R.F. is grateful to Professor Isom Herron (of RPI) for numerous helpful discussions. We also acknowledge the assistance provided in the laboratory by Evgenia Korsukova (University of Nottingham), and for the financial support of a Royal Society travel grant for MRF (Grant No. TG100245) in July 2010, when this work began.

APPENDIX A: DETAILS OF ROSSBY WAVES

1. Overview

As noted in Sec. III F 2, the eigenvalue problem (69) is solved computationally by means of a truncation of the series at N terms. Most of the remarks below are relative to the truncated system.

(a) It is evident from (68b) that $\mathbf{E}^{(m)} = \mathbf{0}$ for all m even, and so $\mathbf{\Phi}^{(m)}$ for m even satisfies the homogeneous equation,

$$\left(\lambda \mathrm{I} + Sg D_m\right)\Phi^{(m)} = \mathbf{0}, \text{ for } m \text{ even}, \tag{A1}$$

so there is a separate eigenvalue problem for m even. However, we shall see below that the initial-value problem indicates that

$$\Phi^{(m)} \equiv \mathbf{0}, m = 2, 4, 6, \ldots. \tag{A2}$$

(b) Equation (29) gives the spectrum of frequencies over a sloping surface that is infinite in the y direction, and for a Fourier series truncated at N terms, there are clearly N^2 eigenvalues, all pure imaginary, and hence $N^2/2$ distinct frequencies. Adding the no-penetration condition at $y = 0$, 1 leads to a spectrum given by solutions of (67) with $\mathbf{E}^{(m)}$ set to zero—ignoring the vertical-flux constraint. Let this problem be denoted by E_0. The eigenvalues for E_0 are easily proved to be pure imaginary. Taking N to be even, there are $N/2$ distinct frequencies for each value of m, and hence there are $N^2/2$ such frequencies. These frequencies appear to always lie in the interval $(0, \sqrt{S})$. Considering only the odd values of m, there are $N^2/4 = \mathcal{N}/2$ frequencies.

(c) Imposing the no-net-flux conditions at lower and upper walls leads to the characteristic equation (75). Taking N to be even as above, and recalling that $\gamma_{mn} = 0$ if either m or n is even, there are $N/2$ terms in the double sum. All terms for a given m combine into a ratio of two polynomials of order N, and since there are $N/2$ such terms, on clearing the fractions, a polynomial of order $N^2/2 \equiv \mathcal{N}$ arises. Therefore, there are here also $\mathcal{N}/2$ frequencies—as for the m-odd E_0 problem.

2. Computational details

As noted, series truncation leads to an eigenvalue equation (75) with the "∞" replaced in each sum by N, leading as noted to a polynomial of order $\mathcal{N}$. So, for a given N, there are $\mathcal{N}$ roots, which all seem to arise as pure-imaginary conjugate pairs, leading then to $\mathcal{N}/2$ distinct frequencies. Computationally, we find that the frequencies range from 0 to an upper limit in the neighborhood of $\sqrt{S}$. In fact, for S large, the matrix D_m takes a simpler form and it may be shown that if one defines $\lambda = \sqrt{S}\lambda'$, then the eigenvalue problem for λ' is S-independent. Further, the frequencies are in some sense close to the frequencies of E_0.

3. Initial conditions

Initially, the solutions given in Secs. III F 1 and III F 2 must be such that C_{mn} and D_{mn} vanish at $t = 0$. First of all, the Rossby-wave modes have $d_{mn} = \mathcal{O}(\eta)$, so the initial condition to leading order involves only the non-wave modes in D_{mn}. Using the form of that solution given in (64), and

evaluating at $\tau = 0$, we obtain

$$\tilde{D}_{mn}(0) = \mathcal{D}_{mn} + \tilde{d}_{mn}(0) = 0, \qquad \tilde{d}_{mn}(0) = \sum_{\beta=1}^{\infty} c_\beta V_{mn\beta}, \quad m, n = 1, 3, 5, 7 \ldots \tag{A3}$$

in the notation given of (62). With series truncation, this becomes a set of $\mathcal{M}$ equations in $\mathcal{M}$ unknowns $\{c_\beta\}$. Hence, the set $\{c_\beta\}$ is in principle determined. Then, the initial value of $\tilde{d}_{mn}$ for this no-wave part of the solution is known and given by (64) and so we may then obtain initial values for $\tilde{c}_{mn}$ corresponding to the no-wave solution. Thus,

$$\tilde{c}_{mn}(0) = -\tanh(\mu_{mn}h)\mathcal{D}_{mn} - \frac{\tanh(\mu_{mn}h)}{4\mu_{mn}^2 Z} \sum_{r=1}^{\infty}\sum_{s=1}^{\infty} \gamma_{rs}\mu_{rs}\Gamma_{rs}\mathcal{D}_{rs}. \tag{A4}$$

Now, we can turn to the Rossby-wave component of the solution. Because there are $\mathcal{N}$ eigenvalues, the general solution for this case is in the form

$$\Phi^{(m)} = \sum_{k=1}^{\mathcal{N}} U_k \mathbf{T}^{(m)}(\lambda_k) e^{\lambda_k \tau}, \tag{A5}$$

where U_k is a constant related to initial conditions. Then, the general solution is

$$C_{mn}(\tau) = \mathcal{C}_{mn} + \frac{1}{\mu_{mn}\sinh(\mu_{mn}h)} \sum_{k=1}^{\mathcal{N}} U_k T_n^{(m)}(\lambda_k) e^{\lambda_k \tau} + \tilde{c}_{mn}(\tau). \tag{A6}$$

Since $C_{mn} = 0$ at $\tau = 0$, to match to the early-time solution, we obtain the set of linear equations for U_k, namely,

$$\sum_{k=1}^{\mathcal{N}} U_k T_n^{(m)}(\lambda_k) = -\mu_{mn}\sinh(\mu_{mn}h)\big[\mathcal{C}_{mn} + \tilde{c}_{mn}(0)\big], \qquad \text{for } m = 1, 3, 5, \ldots, \text{and } n = 1, 2, 3, \ldots, \tag{A7}$$

which is $\mathcal{N}$ equations in $\mathcal{N}$ unknowns. If we introduce the notation

$$\hat{\mathcal{C}}_n^{(m)} = \big[\mathcal{C}_{mn} + \tilde{c}_{mn}(0)\big]\mu_{mn}\sinh(\mu_{mn}h),$$

then this equation may be written in the somewhat more compact form

$$\sum_{k=1}^{\mathcal{N}} U_k \mathbf{T}^{(m)}(\lambda_k) = -\hat{\boldsymbol{\mathcal{C}}}^{(m)}, \; m = 1, 3, 5, \ldots. \tag{A8}$$

More explicitly, this equation may be written in the matrix form

$$\begin{bmatrix} \mathbf{T^{(1)}}(\lambda_\mathbf{1}) & \mathbf{T}^{(1)}(\lambda_2) & \ldots & \mathbf{T}^{(1)}(\lambda_\mathcal{N}) \\ \mathbf{T}^{(3)}(\lambda_1) & \mathbf{T}^{(3)}(\lambda_2) & \ldots & \mathbf{T}^{(3)}(\lambda_\mathcal{N}) \\ \vdots & \vdots & \vdots & \vdots \\ \mathbf{T}^{(N-1)}(\lambda_1) & \mathbf{T}^{(N-1))}(\lambda_2) & \ldots & \mathbf{T}^{(N-1)}(\lambda_\mathcal{N}) \end{bmatrix} \begin{bmatrix} U_1 \\ U_2 \\ \vdots \\ U_\mathcal{N} \end{bmatrix} = - \begin{bmatrix} \hat{\boldsymbol{\mathcal{C}}}^{(1)} \\ \hat{\boldsymbol{\mathcal{C}}}^{(3)} \\ \vdots \\ \hat{\boldsymbol{\mathcal{C}}}^{(N-1)} \end{bmatrix}. \tag{A9}$$

Since each vector $\mathbf{T}^{(m)}$, $\hat{\boldsymbol{\mathcal{C}}}^{(m)}$ has N elements, and there are $N/2$ rows, the matrix at the left is $\mathcal{N} \times \mathcal{N}$. Hence, the set $\{U_k\}$ is in principle determined.

APPENDIX B: DETAILS OF THE COMPUTATION OF ROSSBY WAVE DAMPING

In Sec. III F 3, we obtain a solvability condition for the second-order terms in the asymptotic expansion for the Rossby-wave regime, culminating in an expression (84) for λ_{1j}, the real part of

which is the damping for a Rossby wave with frequency $|\lambda_{0j}|$. The quotient involves integrals of two quantities, $\boldsymbol{\mathcal{S}}_m$ and $\boldsymbol{\mathcal{T}}_m$. From Eq. (82), we find that

$$\boldsymbol{\mathcal{S}}^{(m)} = K_{mj}\left(\lambda_{0j} + Sg\hat{\mathrm{D}}_m\right)\boldsymbol{\Psi}^{(m)} - \frac{\lambda_{0j}}{4}q_m K_{mj}\mathbf{q}\sum_{r=1}^{\infty} q_r \mathbf{q}^{\mathrm{T}}\boldsymbol{\Psi}^{(r)}$$

$$- K_{mj}\mathcal{A}_m\boldsymbol{\Phi}^{(m)} + \frac{q_m K_{mj}\mathbf{q}}{4h}U_{0j} + \frac{K_{mj}\mathbf{H}_m}{4h}\sum_{r=1}^{\infty} q_r\mathbf{q}^{\mathrm{T}}\left(\mathcal{B}_r - \mathrm{I}\right)\boldsymbol{\Psi}^{(r)}, \tag{B1a}$$

$$\boldsymbol{\mathcal{T}}^{(m)} = -K_{mj}\boldsymbol{\Phi}^{(m)} + \frac{\lambda_1}{4}q_m K_{mj}\mathbf{q}U_{0j}. \tag{B1b}$$

Splitting $\boldsymbol{\mathcal{S}}^{(m)}$ into four parts, and simplifying, we have the following:

$$\boldsymbol{\mathcal{S}}_1^{(m)} = \lambda_{0j}K_{mj}\left[\boldsymbol{\Psi}^{(m)} - \frac{q_m\mathbf{q}}{4}\sum_{r=1}^{\infty} q_r\mathbf{q}^{\mathrm{T}}\boldsymbol{\Psi}^{(r)}\right]$$

$$= -K_{mj}\left[\mathcal{A}_m\boldsymbol{\Phi}^{(m)} - \frac{q_m\mathbf{q}}{4}\sum_{r=1}^{\infty} q_r\mathbf{q}^{\mathrm{T}}\mathcal{A}_r\boldsymbol{\Phi}^{(r)}\right], \tag{B2a}$$

$$\boldsymbol{\mathcal{S}}_2^{(m)} = SK_{mj}g\hat{\mathrm{D}}_m\boldsymbol{\Psi}^{(m)} = -\lambda_{0j}^{-1}SK_{mj}g\boldsymbol{\Phi}^{(m)}, \tag{B2b}$$

$$\boldsymbol{\mathcal{S}}_3^{(m)} = \frac{K_{mj}\mathbf{H}_m}{4h}\sum_{r=1}^{\infty} q_r\mathbf{q}^{\mathrm{T}}\left(\mathcal{B}_r - \mathrm{I}\right)\boldsymbol{\Psi}^{(r)} = -\frac{K_{mj}\mathbf{H}_m}{4h}\sum_{r=1}^{\infty} q_r\mathbf{q}^{\mathrm{T}}\left(\mathcal{F}_r - \mathcal{A}_r\right)\boldsymbol{\Phi}^{(r)}, \tag{B2c}$$

$$\boldsymbol{\mathcal{S}}_4^{(m)} = -K_{mj}\mathcal{A}_m\boldsymbol{\Phi}^{(m)} + \frac{q_m K_{mj}\mathbf{q}}{4h}U_{0j}. \tag{B2d}$$

So, $\boldsymbol{\mathcal{S}}^{(m)}$ is the sum of these four quantities. Also,

$$\boldsymbol{\mathcal{T}}^{(m)} = -K_{mj}\boldsymbol{\Phi}^{(m)} + \frac{1}{4}q_m K_{mj}\mathbf{q}U_{0j}. \tag{B3}$$

So, all of terms on the right side of (84) involve summations of the product of $q_m\mathbf{q}^{\mathrm{T}}$. Working through these products, and simplifying, we obtain

$$\sum_{m=1}^{\infty} q_m\mathbf{q}^{\mathrm{T}}\boldsymbol{\mathcal{S}}_1^{(m)} = \frac{1}{4}\chi_1\chi_2 - \chi_3, \tag{B4a}$$

$$\sum_{m=1}^{\infty} q_m\mathbf{q}^{\mathrm{T}}\boldsymbol{\mathcal{S}}_2^{(m)} = -\frac{1}{\lambda_{0j}}\sum_{m=1}^{\infty} q_m\mathbf{q}^{\mathrm{T}}SK_{mj}g\boldsymbol{\Phi}^{(m)}, \tag{B4b}$$

$$\sum_{m=1}^{\infty} q_m\mathbf{q}^{\mathrm{T}}\boldsymbol{\mathcal{S}}_3^{(m)} = -\frac{\chi_5 - \chi_1}{4h}\sum_{m=1}^{\infty} q_m\mathbf{q}^{\mathrm{T}}K_{mj}\mathbf{H}_m, \tag{B4c}$$

$$\sum_{m=1}^{\infty} q_m\mathbf{q}^{\mathrm{T}}\boldsymbol{\mathcal{S}}_4^{(m)} = \frac{1}{4h}U_{0j}\chi_2 - \chi_3, \tag{B4d}$$

where

$$\chi_1 = \sum_{r=1}^{\infty} q_r\mathbf{q}^{\mathrm{T}}\mathcal{A}_r\boldsymbol{\Phi}^{(r)}, \quad \chi_2 = \sum_{r=1}^{\infty} q_r^2\mathbf{q}^{\mathrm{T}}K_{rj}\mathbf{q}, \quad \chi_3 = \sum_{r=1}^{\infty} q_r\mathbf{q}^{\mathrm{T}}K_{rj}\mathcal{A}_r\boldsymbol{\Phi}^{(r)},$$

$$\chi_4 = \sum_{r=1}^{\infty} q_r\mathbf{q}^{\mathrm{T}}K_{rj}\boldsymbol{\Phi}^{(r)}, \quad \chi_5 = \sum_{r=1}^{\infty} q_r\mathbf{q}^{\mathrm{T}}\mathcal{F}_r\boldsymbol{\Phi}^{(r)}.$$

Further,

$$\sum_{m=1}^{\infty} q_m \mathbf{q}^{\mathrm{T}} \boldsymbol{\mathcal{T}}^{(m)} = -\chi_4 + \frac{1}{4}\chi_2\, U_{0j}. \tag{B5}$$

Recall that there is a problem in computing some of the above sums. In particular, χ_1 and χ_3 are divergent series, based on the solutions obtained in Sec. III F 2. (The denominator of (84) is bounded, since it does not depend on χ_1 and χ_3.) As noted in Sec. III F 3, this divergence arises because of the very slow decay of $\mathbf{\Phi}^{(m)}$, which goes like $q_m\mathbf{q}$ for $m \to \infty$, and that behavior may be traced to the neglect of a particular term in (55c). Retention of the term replaces eigenvalue problem (69) with

$$\left(\lambda_0 \mathrm{I} + Sg\mathrm{D}_m + \eta \mathcal{A}_m\right)\mathbf{\Phi}^{(m)} = \mathbf{E}^{(m)} U. \tag{B6}$$

The final term inside the left-hand-side parentheses leads to a $\mathbf{\Phi}^{(m)}$ behaviour for large m of $q_m^2\mathbf{q}$, which is sufficient to guarantee convergence of all of the above series.

There are small corrections to the damping formulae that arise by retaining other terms of comparable order. The linear operator K_{mj} originally defined in (81) is now

$$K_{mj} \equiv \left(\lambda_{0j}\mathrm{I} + Sg\mathrm{D}_m + \eta\mathcal{A}_m\right)^{-1}. \tag{B7}$$

The term $\eta\mu_{mk}^2 \sinh(\mu_{mk}h)d_{mk}$ in (55c) must also be retained; the only impact of that addition is to modify $\boldsymbol{\mathcal{S}}_2^{(m)}$, so one of the above sums is altered, namely,

$$\sum_{m=1}^{\infty} q_m \mathbf{q}^{\mathrm{T}} \boldsymbol{\mathcal{S}}_2^{(m)} = -\frac{1}{\lambda_{0j}}\left[\sum_{m=1}^{\infty} q_m \mathbf{q}^{\mathrm{T}} K_{mj}\left(Sg + \eta\mathcal{M}^{(m)}\right)\mathbf{\Phi}^{(m)}\right], \qquad \mathcal{M}^{(m)} = [\delta_{ij}\mu_{mi}^2]. \tag{B8}$$

In order for this large-m behaviour to be manifest, we clearly require that the final term be largest for large m, hence the requirement on the number of terms in the truncated series, N, namely,

$$\lambda_0 \ll \mathcal{O}(N\eta). \tag{B9}$$

So, if λ_0 is order one, for a given value of η, one must take $N \gg \eta^{-1}$. Typically, in the computations done in order to generate the numbers in Table IV, we took values of η from 0.1 to 0.01, and for each η value, computed values of λ_1 for $N = 100$, 150, and 200, and 250 for some cases. A least-squares scheme, for $\lambda_1 \sim c_1 + c_2/N$ then determined an extrapolated value for $N = \infty$, that is, c_1.

Once reliable, N-extrapolated values for λ_1 were obtained, we found that the numbers are very well fit by taking, for a particular eigenvalue, λ_{0k},

$$\lambda_{1k} = a_k(S) + b_k(S)\log\eta. \tag{B10}$$

Figure 9 shows this fit plotted with results of calculations for particular η values, for two examples corresponding to differing values of S.

The members of $\{\chi_k\}$ that are unbounded for $\eta \to 0$ may be decomposed into convergent and divergent sums at $\eta = 0$. For example, for χ_1, it may be shown by examining the large-m behaviour of $\mathbf{\Phi}^{(m)}$ that

$$\chi_1(\eta) = \chi_{1o}(\eta) + \frac{\lambda_o U\sqrt{S}}{\pi^2}|\mathbf{q}|^2 \sum_{m=1}^{\infty} \frac{1}{m(\lambda_o + m\eta\sqrt{S})}, \qquad |\chi_{1o}(0)| < R,$$

where R is some positive number. Using the fact that λ_o is pure imaginary, we simplify the final term and incorporate the bounded portion of the sum into χ_{1o} as χ'_{1o}. Then,

$$\chi_1(\eta) = \chi'_{1o}(\eta) + \chi_{1s}(\eta), \quad \chi_{1s}(\eta) \equiv \frac{|\lambda_o|^2 U\sqrt{S}}{\pi^2}|\mathbf{q}|^2 \sum_{m=1}^{\infty} \frac{1}{m(|\lambda_o|^2 + m^2 S\eta^2)}.$$

It turns out that[22]

$$\chi_{1s}(\eta) = \frac{U\sqrt{S}}{\pi^2}|\mathbf{q}|^2\left[\gamma + \Re eal\left\{\psi\left(1 + i\frac{|\lambda_o|}{\sqrt{S}\,\eta}\right)\right\}\right],$$

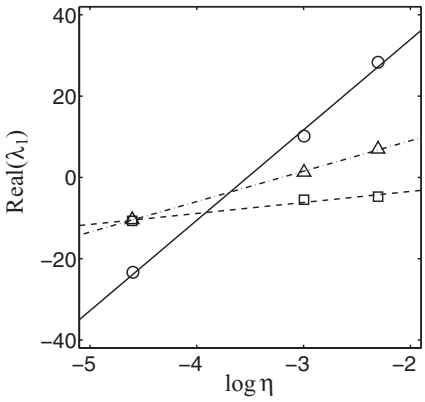

FIG. 9. Computations of the real part of λ_1 versus $\log \eta$. For $\circ$, $S = 5.0$, $|\lambda_0| = 0.948$; for $\triangle$, $S = 1.0$, $|\lambda_0| = 0.497$; for $\square$, $S = 0.5$, $|\lambda_0| = 0.710$. Each point represents an N-extrapolated value. The straight lines are least-squares fits using $a + b\log \eta$ for each case. It is also evident that the damping at very small η is much less for $S = 0.5$ than for $S = 2.0$.

where γ is the Euler constant and the Digamma function is $\psi(z) \equiv \Gamma'(z)/\Gamma(z)$. A standard asymptotic formula[22] gives

$$\chi_{1s}(\eta) \sim \frac{U\sqrt{S}}{\pi^2}|\mathbf{q}|^2\Big[-\log\eta + \gamma + \log(|\lambda_o|/\sqrt{S}) + \gamma + \mathcal{O}(\eta^2)\Big], \quad \eta \to 0.$$

Thus, we have proved that χ_1 does indeed have a logarithmic behavior for $\eta \to 0$. A similar analysis may be done for χ_3, which can be seen to have a form much like that for χ_1. Combined with all of the other terms comprising the numerator of (84), including the components of χ_1 that are finite at $\eta = 0$, Eq. (B10) is not arbitrary, but fully justified.

[1] H. P. Greenspan and L. N. Howard, "On a time-dependent motion of a rotating fluid," J. Fluid Mech. **17**, 385–404 (1963).
[2] E. R. Benton and A. Clark, "Spin-up," Annu. Rev. Fluid Mech. **6**, 257–280 (1974).
[3] P. W. Duck and M. R. Foster, "Spin-up of homogeneous and stratified fluids," Annu. Rev. Fluid Mech. **33**, 231–263 (2001).
[4] K. Stewartson, "On almost rigid rotations," J. Fluid Mech. **3**, 17–26 (1957).
[5] G. Walin, "Some aspects of time-dependent motion of a stratified rotating fluid," J. Fluid Mech. **36**(2), 289–307 (1969).
[6] T. Sakurai, "Spin down problem of rotating stratified fluid in thermally insulated circular cylinders," J. Fluid Mech. **37**(4), 689–699 (1969).
[7] R. E. Hewitt, M. R. Foster, and P. A. Davies, "Spin-up of a two-layer rotating stratified fluid in a variable-depth container," J. Fluid Mech. **438**, 379–407 (2001).
[8] R. E. Hewitt, P. W. Duck, and M. R. Foster, "Steady boundary-layer solutions for a swirling stratified fluid in a rotating cone," J. Fluid Mech. **384**, 339–374 (1999).
[9] R. E. Hewitt, P. A. Davies, P. W. Duck, and M. R. Foster, "Spin-up of stratified rotating flows at large Schmidt number: experiment and theory," J. Fluid Mech. **389**, 169–207 (1999).
[10] J. Pedlosky and H. P. Greenspan, "A simple laboratory model for the oceanic circulation," J. Fluid Mech. **27**, 291–304 (1967).
[11] G. J. F. van Heijst, "Spin-up phenomena in non-axisymmetric containers," J. Fluid Mech. **206**, 171–191 (1989).
[12] G. J. F. van Heijst, P. A. Davies, and R. G. Davis, "Spin-up in a rectangular container," Phys. Fluids A **2**, 150–159 (1990).
[13] G. J. F. van Heijst, L. R. M. Maas, and C. W. M. Williams, "The spin-up of fluid in a rectangular container with a sloping bottom," J. Fluid Mech. **265**, 125–159 (1994).
[14] M. R. Foster and R. J. Munro, "The linear spin-up of a stratified, rotating fluid in a square cylinder," J. Fluid Mech. **712**, 7–40 (2012).
[15] G. S. M. Spence, M. R. Foster, and P. A. Davies, "The transient response of a contained rotating stratified fluid to impulsive surface forcing," J. Fluid Mech. **243**, 33–50 (1992).
[16] R. J. Munro, M. R. Foster, and P. A. Davies, "Instabilities in the spin-up of a rotating, stratified fluid," Phys. Fluids **22**, 054108 (2010).
[17] G. F. Carnevale, R. C. Kloosterziel, and G. J. F. van Heijst, "Propagation of barotropic vortices over topography in a rotating tank," J. Fluid Mech. **233**, 119–139 (1991).
[18] J. Pedlosky, *Geophysical Fluid Dynamics* (Springer, New York, 1982).
[19] P. Rhines, "Edge-, bottom-, and Rossby waves in a rotating stratified fluid," Geophys. Fluid Dyn. **1**, 273–302 (1970).
[20] J. A. van de Konijnenberg and G. J. F. van Heijst, "Free-surface effects on spin-up in a rectangular tank," J. Fluid Mech. **334**, 189–210 (1997).
[21] J. A. van de Konijnenberg, J. B. Flor, and G. J. F. van Heijst, "Decaying quasi-two-dimensional viscous flow on a square domain," Phys. Fluids **10**(2), 595–606 (1998).
[22] P. J. Davis, "Gamma function and related functions," in *Handbook of Mathematical Functions*, edited by M. Abramowitz and I. Stegun (National Bureau of Standards, Washington, DC, 1954), pp. 258–259.